INTERNATIONAL JOURNAL FOR NUMERICAL METHODS IN BIOMEDICAL ENGINEERING
Int. J. Numer. Meth. Biomed. Engng. 2014; **30**:1238–1262
Published online 28 July 2014 in Wiley Online Library (wileyonlinelibrary.com). DOI: 10.1002/cnm.2654

Elastic–viscoplastic modeling of soft biological tissues using a mixed finite element formulation based on the relative deformation gradient

J. Weickenmeier[1] and M. Jabareen[2,*,†]

[1]*Department of Mechanical and Process Engineering, ETH Zurich, Zurich, Switzerland*
[2]*Faculty of Civil and Environmental Engineering, Technion—Israel Institute of Technology, Haifa, Israel*

SUMMARY

The characteristic highly nonlinear, time-dependent, and often inelastic material response of soft biological tissues can be expressed in a set of elastic–viscoplastic constitutive equations. The specific elastic–viscoplastic model for soft tissues proposed by Rubin and Bodner (2002) is generalized with respect to the constitutive equations for the scalar quantity of the rate of inelasticity and the hardening parameter in order to represent a general framework for elastic–viscoplastic models. A strongly objective integration scheme and a new mixed finite element formulation were developed based on the introduction of the relative deformation gradient—the deformation mapping between the last converged and current configurations. The numerical implementation of both the generalized framework and the specific Rubin and Bodner model is presented. As an example of a challenging application of the new model equations, the mechanical response of facial skin tissue is characterized through an experimental campaign based on the suction method. The measurement data are used for the identification of a suitable set of model parameters that well represents the experimentally observed tissue behavior. Two different measurement protocols were defined to address specific tissue properties with respect to the instantaneous tissue response, inelasticity, and tissue recovery. Copyright © 2014 John Wiley & Sons, Ltd.

Received 21 February 2014; Revised 27 April 2014; Accepted 4 May 2014

KEY WORDS: soft tissue; viscoplasticity; mixed finite element formulation; Cutometer measurements; inverse problem

1. INTRODUCTION

Understanding the mechanical response of soft biological tissues is essential in the development of computational tools to enable physically based simulations for realistic applications in the medical field. This includes the planning of surgical interventions, the design of biocompatible prosthetic devices and implants, and the quantitative evaluation of different medical treatments with respect to faster healing of diseased and damaged tissue. Mathematical modeling in general and the finite element (FE) method in particular are crucial tools in understanding the mechanical response of soft biological tissues. Specifically, the FE method can be used in simulations of organs and systems of organs at increasing levels of complexity with respect to the level of structural representation, material models across different length scales, interaction of multiple tissue structures, and the type of medical application.

Generally speaking, soft tissues differ by their specific composition of mostly collagen, elastin, and a hydrated matrix of proteoglycans, as well as other constituents depending on their individual functionality. Experimental observations have shown that soft biological tissues exhibit a highly

*Correspondence to: M. Jabareen, Faculty of Civil and Environmental Engineering, Technion—Israel Institute of Technology, Haifa, Israel.
†E-mail: cvjmah@tx.technion.ac.il

nonlinear response, pronounced anisotropy, heterogeneous and large deformation upon physiological loading, hysteresis, and often a poroelastic and (nearly) incompressible material response [1]. Additionally, soft biological tissues exhibit a strong time-dependent and history-dependent behavior governed by fluid flow through porous fibrous networks, presence of transient fiber network connections, and inherent time-dependent behavior of tissue components (e.g., elastin and collagen) [2]. Alongside these effects, tissues undergo different forms of morphological changes over time, leading to irreversible deformations and altered morphology. Such effects are seen in pre-conditioning in cyclically loaded soft tissues [1, 3, 4]; stress relaxation at constant strain [5]; growth of skin, heart, tumor, and muscle tissues [6–8]; softening of stretched tissue [4, 9, 10]; damage [11–14]; and collagen turnover, remodeling, and aging [15–18].

In constitutive modeling of time-dependent and history-dependent material, the mechanical behavior is generally differentiated by viscoelasticity and inelasticity. Among the most frequently used formulations for rate-dependent stress response of soft biological tissues are Fung-type quasi-linear viscoelastic models [1]. The extensive flexibility with respect to constitutive formulations for the rate of instantaneous elastic stress and the reduced relaxation function in the hereditary integral of the viscoelastic stress inspired several specific formulations for tendons [19, 20], collagenous tissue [21], skin [22], human liver [23], and ligaments [24] among many other applications. However, these models are of purely phenomenological nature and often fail to properly describe the characteristic highly nonlinear behavior [20].

Another common approach was adopted for studying skin tissue [22], as well as viscoelastic soft fiber-reinforced composites [25] and the cornea [26], which is based on a multiplicative decomposition of the deformation gradient into an elastic and viscous part. In this approach, evolution equations are determined for strain-like internal variables. In contrast, work has been presented in formulating rate equations for stress-like internal variables solved by means of convolution equations, as presented by Holzapfel and Simo [27] and Govindjee and Reese [28]. Applications of this approach were presented by Holzapfel *et al.* [29, 30] for arterial tissue, as well as by Peña *et al.* [31, 32] for ligaments.

Despite several well-justified constitutive assumptions, viscoelasticity fails to describe the strongly apparent inelastic response of soft biological tissues [1]. Literature provides experimental evidence for several different softening phenomena related to damage and loading beyond the physiological state of tissue (e.g., [33–35] and references therein). Constitutive models for the description of irreversible alterations of tissue on the structural level have been proposed for fiber-reinforced tissues [36, 37] alongside the aforementioned work. The respective work has revealed a similar softening behavior as it was described by Mullins [38] for rubber-like materials, in particular for modeling tissues beyond their physiological limit [33]. Furthermore, softening in soft tissues is related to transient adaptation of tissue structure to certain loads, maturation, remodeling, and fiber reorientation. Preconditioning due to cyclic loading of tissues [3, 39], as well as creep [40] and skin relaxation experiments [41], demonstrates the necessity to include different softening mechanisms when aiming at realistic modeling of soft tissues [4, 19, 33, 42, 43]. However, a final aspect often related to softening is residual strains accumulating not only in the pathological but also in the physiological regime. Different work is presented in the literature expressing tissue softening and corresponding irreversible deformations within mathematical formulations [10, 44–46], as well as in combination with damage models [36, 47–49].

To the best of the author's knowledge, few works have been presented on the basis of elastic–viscoplastic theory despite the significant freedom of capturing nearly all of the characteristic properties of soft biological tissues (e.g., [46, 50]). In the work presented by Rubin and Bodner [46], the elastic strain part as well as the dissipative tissue response is governed by evolution equations. This model considers the typically observed accumulation of residual strain and softening behavior from the first loading cycle onwards. Moreover, the constitutive equations are formulated in terms of the deformed metric, recognizing the fact that elastic deformation should be associated with the current configuration during plastic flow [51–54]. In recent years, the Rubin and Bodner model was adopted for FE modeling of facial tissues [41, 55].

The objective of the present paper is the mathematical formulation of a set of generalized elastic–viscoplastic constitutive equations for the inelastic modeling of soft biological tissues within a

DOI: 10.1002/cnm

corresponding FE formulation. In particular, constitutive equations that are based on the rate forms of the deformation measures require a strongly objective integration scheme and a proper FE formulation. For this reason, a new mixed formulation is proposed that is formulated in terms of the last converged and current configurations. In view of these configurations, the *relative deformation gradient* is introduced, which plays a crucial role in all subsequent derivations presented in this paper.

The outline of the paper is as follows. Section 2 presents a generalized framework for the elastic–viscoplastic constitutive formulation of soft biological tissues and summarizes the constitutive model equations introduced by Rubin and Bodner [46]. Section 3 presents the strongly objective integration scheme, and in Section 4, the consistent spatial tangent moduli are derived. In Section 5, the new mixed FE formulation is introduced. Section 6 presents the validation for the FE formulation through standard tests, and Section 7 describes an experimental campaign of Cutometer measurements, which is used to demonstrate a procedure to determine a set of model parameters for facial skin tissue. Finally, Section 8 summarizes and concludes the present study.

2. CONSTITUTIVE MODEL FORMULATION

By way of background, let $\mathbf{X}^{\ddagger}$ denote the location of a material point in the reference configuration, $\mathbf{x}$ the location of the same material point in the present configuration at time t, and $\mathbf{v} = \dot{\mathbf{x}}$ the absolute velocity of a material point. Here and throughout the text, a superposed dot is used to denote material time differentiation, where $\mathbf{X}$ is fixed. Furthermore, let $\mathbf{F} = \partial\mathbf{x}/\partial\mathbf{X}$ be the deformation gradient, $\mathbf{l} = \partial\mathbf{v}/\partial\mathbf{x}$ be the velocity gradient, $\mathbf{d} = (\mathbf{l} + \mathbf{l}^{\mathsf{T}})/2$ be the rate of deformation tensor, and $\mathbf{b} = \mathbf{F}\mathbf{F}^{\mathsf{T}}$ be the total deformation tensor.

Following the work of Eckart [51], Besseling [56], Leonov [57], and Rubin *et al.* [46, 52], it is possible to model inelastic response by introducing an elastic distortional deformation tensor associated with a dissipative response as a primary quantity governed by an evolution equation. In particular, the total dilatation J, the measure of the total elastic distortional deformation $\mathbf{b}'$, and the elastic distortional deformation associated with the dissipative component $\mathbf{b}'_{de}$ are specified by the following evolution equations [46]:

$$\begin{aligned} \dot{J} &= J\,\mathbf{d}\colon\mathbf{I}, \\ \dot{\mathbf{b}}' &= \mathbf{l}\mathbf{b}' + \mathbf{b}'\mathbf{l}^{\mathsf{T}} - \frac{2}{3}(\mathbf{d}\colon\mathbf{I})\mathbf{b}', \\ \dot{\mathbf{b}}'_{de} &= \mathbf{l}\mathbf{b}'_{de} + \mathbf{b}'_{de}\mathbf{l}^{\mathsf{T}} - \frac{2}{3}(\mathbf{d}\colon\mathbf{I})\mathbf{b}'_{de} - \Gamma\mathbf{a}_d, \quad \mathbf{a}_d = \mathbf{b}'_{de} - \frac{3}{\mathbf{b}'^{-1}_{de}\colon\mathbf{I}}\mathbf{I}, \end{aligned} \tag{1}$$

where the first two evolution equations in (1) control the elastic response, while the third evolution equation controls the inelastic response. Specifically, the term $\Gamma\mathbf{a}_d$ in $(1c)$ models the rate of inelastic deformation, with $\mathbf{a}_d$ being the direction of inelastic flow and Γ being the magnitude of the rate of inelasticity. In this regard, it is noted that when $\Gamma\mathbf{a}_d$ vanishes, the dissipative component responds elastically. Furthermore, the form of the symmetric tensor $\mathbf{a}_d$ in $(1d)$ is one of the simplest forms, which ensures the elastic distortional deformation tensor associated with the dissipative component, $\mathbf{b}'_{de}$, to remain a unimodular tensor and to evolve toward the value $\mathbf{I}$.

2.1. General elastic–viscoplastic constitutive equations for soft biological tissue

In this section, the scalar of the rate of inelasticity as well as the hardening parameter are presented in a general form because these mechanical mechanisms are usually tissue dependent. Based on experimental observations of a specific tissue (e.g., the Rubin and Bodner model for facial tissue), one can propose an explicit form for the functions Γ and $\dot{\beta}$. Specifically, the nonnegative function Γ is proposed in the following general form

[‡]Please see Appendix A for a list of variables and symbols.

DOI: 10.1002/cnm

$$\Gamma = \widehat{\Gamma}(\dot{\varepsilon},\, \beta,\, \beta_{de}), \tag{2}$$

where $\dot{\varepsilon}$ is the effective total distortional deformation rate and β_{de} is the effective elastic distortion strain associated with the dissipative component. The magnitude of the rate of inelasticity Γ serves as a continuous switch where the plastic deformation evolves continuously with a smooth transition from elastic to plastic responses. In this regard, a more general form for the scalar function Γ can be obtained by replacing β_{de} by the two invariants of the unimodular tensor $\mathbf{b}'_{de}$ and also by adding the dependency over the two invariants of the unimodular tensor $\mathbf{b}'$.

The scalars $\{\dot{\varepsilon},\, \beta_{de}\}$ are, respectively, defined by

$$\dot{\varepsilon} = \sqrt{\frac{2}{3}}\|\mathrm{dev}\,(\mathbf{d})\,\|, \quad \beta_{de} = \sqrt{\frac{3}{2}}\|\mathrm{dev}\,(\mathbf{b}'_{de})\,\|, \tag{3}$$

where $\|\,\bullet\,\| = \sqrt{\bullet\!:\!\bullet}$ is the norm operator and $\mathrm{dev}\,(\bullet) = \bullet - 1/3\,(\bullet\!:\mathbf{I})\,\mathbf{I}$ is the deviator operator. Furthermore, the scalar valued function β in (2) is a hardening measure, which can be associated with fluid flow through cells of the tissue for example and is given by an evolution equation of the following general form

$$\dot{\beta} = \widehat{\beta}\,(\dot{\varepsilon},\, \Gamma,\, \beta,\, \beta_{de})\,. \tag{4}$$

The unspecified functional forms of $\widehat{\Gamma}$ and $\widehat{\beta}$ may be defined to properly represent a specific tissue response. Moreover, their unspecified form allows us to derive a general numerical framework for elastic–viscoplastic models.

Now, a full set of evolution equations is formulated for $\{J,\, \mathbf{b}',\, \mathbf{b}'_{de},\, \beta\}$, and appropriate initial conditions are needed in order to fully describe the initial-boundary value problem. Assuming that the material is in the virgin state at the start time $t = t_0$, then the initial conditions are specified by

$$J\,(t_0) = 1, \quad \mathbf{b}'\,(t_0) = \mathbf{I}, \quad \mathbf{b}'_{de}\,(t_0) = \mathbf{I}, \quad \beta\,(t_0) = \beta_0. \tag{5}$$

It should be noted that if Equations (1c) and (4) are homogeneous of order 1 in time, then the model will predict a rate-independent elastic–plastic response.

Next, the strain energy function W, which accounts for the stored elastic energy per undeformed unit volume, is based on the work by Rubin and Bodner [46] and is therefore proposed as a function of the total dilatation $J = \det(\mathbf{F})$, with four invariants, two of which are based on the total deformation tensor $\{\beta_1 = \mathbf{b}'\!:\mathbf{I},\ \beta_2 = \mathbf{b}'\!:\mathbf{b}'\}$ and the other two on the dissipative component $\{\alpha_1 = \mathbf{b}'_{de}\!:\mathbf{I},\ \alpha_2 = \mathbf{b}'_{de}\!:\mathbf{b}'_{de}\}$, and the stretch of the I'th fiber family $\lambda_I = \|\mathbf{m}_I\|,\ I = 1, \ldots, N_{\text{fib.}}$ (where $\mathbf{m}_I = \mathbf{F}\cdot\mathbf{M}_I$ is a vector characterizing the orientation and the stretch of the I'th fiber family and M_I is a unit vector characterizing the reference orientation of the same fiber family). The general form of the strain energy function is specified by

$$W = \widehat{W}\,(J,\, \beta_1,\, \beta_2,\, \alpha_1,\, \alpha_2,\, \lambda_I)\,. \tag{6}$$

Within the context of the purely mechanical theory that states the positiveness of the rate of material dissipation, $\mathsf{D} = \boldsymbol{\sigma}\!:\mathbf{d} - \dot{W}/J \geqslant 0$, the Cauchy stress tensor reads

$$\begin{aligned}\boldsymbol{\sigma} = {} & \frac{\partial W}{\partial J}\mathbf{I} + \frac{2}{J}\frac{\partial W}{\partial \beta_1}\mathrm{dev}\,(\mathbf{b}') + \frac{4}{J}\frac{\partial W}{\partial \beta_2}\mathrm{dev}\,(\mathbf{b}'^2) \\ & + \frac{2}{J}\frac{\partial W}{\partial \alpha_1}\mathrm{dev}\,(\mathbf{b}'_{de}) + \frac{4}{J}\frac{\partial W}{\partial \alpha_2}\mathrm{dev}\,(\mathbf{b}'^2_{de}) + \sum_{I=1}^{N_{\text{fib.}}}\frac{1}{J\lambda_I}\frac{\partial W}{\partial \lambda_I}\mathbf{m}_I \otimes \mathbf{m}_I\,.\end{aligned} \tag{7}$$

It should be noted that a different constitutive formulation for the rate of deformation tensor $\mathbf{d}$ would lead to a different functional form of the Cauchy stress tensor $\boldsymbol{\sigma}$ as was presented by Papes [58].

DOI: 10.1002/cnm

2.2. *Specific elastic–viscoplastic constitutive equations for soft biological tissues—Rubin and Bodner model*

Rubin and Bodner [46] developed three-dimensional constitutive equations that describe finite elastic–viscoplastic deformations that produce reasonable agreement with experimental data of facial tissues. In particular, the specific constitutive equation for the magnitude of the rate of inelasticity Γ is given by

$$\Gamma = (\Gamma_1 + \Gamma_2 \dot{\varepsilon})\, exp\left(-\frac{1}{2}\left(\frac{\beta}{\beta_{de}}\right)^{2n}\right), \tag{8}$$

where $\{\Gamma_1, \Gamma_2, n\}$ are material parameters of which Γ_1 controls the rate-dependent inelastic response, while $\Gamma_2 \dot{\varepsilon}$ controls the rate-independent inelastic response and n controls the sharpness of the elastic–plastic transition. The hardening function is specified by the evolution equation

$$\dot{\beta} = \frac{r_1 r_3 + r_2 \dot{\varepsilon}}{r_3 + \dot{\varepsilon}} \Gamma \beta_{de} - r_4 \beta^{r_5}, \tag{9}$$

where the constants $\{r_1, \ldots, r_5\}$ are material parameters. Specifically, r_1 controls the rate of hardening during relaxation (i.e., $\dot{\varepsilon} = 0$), r_2 controls the rate of hardening during loading (i.e., $\dot{\varepsilon} > 0$), and r_3 controls the value of strain rate associated with the transition between these two responses. Note that the first part on the right-hand side of (9) causes β to grow, while the second part is responsible for material recovery. The parameters $\{r_4, r_5\}$ control the rate and shape of recovery of hardening, respectively. Furthermore, it is worth noting that the rate of inelastic deformation yields a rate-independent response, when the following conditions are fulfilled

$$\Gamma_2 \dot{\varepsilon} \gg \Gamma_1, \quad r_2 \dot{\varepsilon} \gg r_1 r_3, \quad \dot{\varepsilon} \gg r_3, \quad r_4 = 0. \tag{10}$$

The strain energy function proposed by Rubin and Bodner [46] models tissues as a composite material composed of an elastic material, elastic fibers, and a dissipative elastic–viscoplastic material. The specific form of the proposed strain energy function W is given by

$$W = \frac{\mu_0}{2q}\left(e^{qg} - 1\right), \tag{11}$$

where μ_0 and q are material parameters, and the function $g = \widehat{g}\,(J, \beta_1, \lambda_I, \alpha_1)$ was decoupled into four parts such that

$$\begin{aligned} \widehat{g}\,(J, \beta_1, \lambda_I, \alpha_1) &= \widehat{g}_1\,(J) + \widehat{g}_2\,(\beta_1) + \widehat{g}_3\,(\lambda_I) + \widehat{g}_4\,(\alpha_1), \\ \widehat{g}_1\,(J) &= 2m_1\,(J - 1 - ln\,(J)), \quad \widehat{g}_2\,(\beta_1) = m_2\,(\beta_1 - 3), \\ \widehat{g}_3\,(\lambda_I) &= \frac{m_3}{m_4}\sum_{I=1}^{N_{\text{fib.}}} \langle \lambda_I - 1 \rangle^{2m_4}, \quad \widehat{g}_4\,(\alpha_1) = m_5\,(\alpha_1 - 3), \end{aligned} \tag{12}$$

where $\{m_1, \ldots, m_5\}$ are additional material parameters. The individual parts of g include the function $\widehat{g}_1\,(J)$ accounting for total volume dilatation, $\widehat{g}_2\,(\beta_1)$ accounting for the distortional deformation of the isotropic matrix, $\widehat{g}_3\,(\lambda_I)$ accounting for the stretch of the I'th fiber family, and $\widehat{g}_4\,(\alpha_1)$ accounting for the elastic distortional deformation of the dissipative component of the tissue. In (12d), $\langle \bullet \rangle = (|\bullet| + \bullet)/2$ are the McAuley brackets that eliminate the response of the I'th fiber family if under compression. Now using (7), it can be shown that the Cauchy stress tensor is given by

$$\boldsymbol{\sigma} = \frac{\mu}{J}\left[m_1\,(J-1)\,\mathbf{I} + m_2 \text{dev}\left(\mathbf{b}'\right) + m_3 \sum_{I=1}^{N_{\text{fib.}}} \frac{\langle \lambda_I - 1 \rangle^{2m_4 - 1}}{\lambda_I} \mathbf{m}_I \otimes \mathbf{m}_I + m_5 \text{dev}\left(\mathbf{b}'_{de}\right)\right], \tag{13}$$

where μ is the nonlinear shear modulus and is defined by

$$\mu = \mu_0 e^{qg}. \tag{14}$$

DOI: 10.1002/cnm

3. STRESS UPDATE AND INTERNAL VARIABLE INTEGRATION SCHEME

Typically, the evolution equations for elastic–viscoplastic response of metals tend to be stiff differential equations that require special methods of integration to obtain a stable response. Integration algorithms for evolution equations of the elastic measures of the deformation have been discussed by Rubin and Attia [52]. More recently, Rubin and Papes [59] developed a strongly objective integration algorithm for viscoplastic models governed by evolution equations of the elastic measure of the deformation. In this section, the strongly objective integration algorithm presented by Rubin and Papes [59] is applied for integrating (1) and (4).

In particular, considering a time increment that begins at time t_n and ends at t_{n+1} with time interval $\Delta t = t_{n+1} - t_n$ and assuming that the solutions of $\left\{J(t_n),\ \mathbf{b}'(t_n),\ \mathbf{b}'_{de}(t_n),\ \beta(t_n)\right\}$ at time t_n are known, the numerical algorithm must provide $\left\{J(t_{n+1}),\ \mathbf{b}'(t_{n+1}),\ \mathbf{b}'_{de}(t_{n+1}),\ \beta(t_{n+1})\right\}$ at time t_{n+1}. The strongly objective integration algorithm for the evolution equations of the measures of deformation $\left\{J,\ \mathbf{b}',\ \mathbf{b}'_{de},\ \beta\right\}$ ensures that the values of the tensors $\left\{\mathbf{b}'(t_{n+1}),\ \mathbf{b}'_{de}(t_{n+1})\right\}$ at time increment t_{n+1} have the same invariance properties under superposed rigid body motion (SRBM) as the exact tensors $\left\{\mathbf{b}',\ \mathbf{b}'_{de}\right\}$, when $\{J(t_{n+1}),\ \beta(t_{n+1})\}$ are unaffected by the SRBM. To this end, use is made of the work by Rubin and Papes [59] and Simo [60, 61] to develop a relative deformation gradient. Specifically, the relative deformation gradient $\mathbf{F}_r$, its determinant J_r, and the unimodular part of the relative deformation gradient $\mathbf{F}'_r$ are defined by

$$\begin{aligned}
&\mathbf{F}_r = \frac{\partial \mathbf{x}\,(t)}{\partial \mathbf{x}\,(t_n)}, \quad \dot{\mathbf{F}}_r = \mathbf{l}\mathbf{F}_r, \quad \mathbf{F}_r\,(t_n) = \mathbf{I},\\
&J_r = \det\left(\mathbf{F}_r\right), \quad \dot{J}_r = J_r\mathbf{d}\colon\mathbf{I}, \quad J_r\,(t_n) = 1,\\
&\mathbf{F}'_r = J_r^{-1/3}\mathbf{F}_r, \quad \dot{\mathbf{F}}'_r = \operatorname{dev}(\mathbf{l})\,\mathbf{F}'_r, \quad \mathbf{F}'_r\,(t_n) = \mathbf{I}.
\end{aligned} \tag{15}$$

Then, the exact solution of $(1a, b)$ and the approximated solution of $(1c)$ are given by

$$\begin{aligned}
J\,(t_{n+1}) &= J_r\,(t_{n+1})\,J\,(t_n)\,,\\
\mathbf{b}'\,(t_{n+1}) &= \mathbf{F}'_r\,(t_{n+1})\,\mathbf{b}'\,(t_n)\,\mathbf{F}'^{\mathsf{T}}_r\,(t_{n+1})\,,\\
\mathbf{b}'_{de}\,(t_{n+1}) &= \mathbf{b}'^{*}_{de}\,(t_{n+1}) - \Delta t\,\Gamma\,(t_{n+1})\,\mathbf{a}_d\,(t_{n+1})\,,
\end{aligned} \tag{16}$$

where $\mathbf{b}'^{*}_{de}\,(t_{n+1})$ is the elastic trial solution of the elastic distortional deformation of the dissipative component and is defined by

$$\mathbf{b}'^{*}_{de}\,(t_{n+1}) = \mathbf{F}'_r\,(t_{n+1})\,\mathbf{b}'_{de}\,(t_n)\,\mathbf{F}'^{\mathsf{T}}_r\,(t_{n+1})\,. \tag{17}$$

Bearing in mind that the deviatoric part of the tensor $\mathbf{a}_d$ is identical to the deviatoric part of $\mathbf{b}'_{de}$ (according to $(1d)$) and using $(3b)$, it can be shown that

$$\begin{aligned}
\operatorname{dev}\left(\mathbf{b}'_{de}\,(t_{n+1})\right) &= \frac{1}{1+\Delta t\,\Gamma\,(t_{n+1})}\operatorname{dev}\left(\mathbf{b}'^{*}_{de}(t_{n+1})\right),\\
\beta_{de}\,(t_{n+1}) &= \frac{\beta^{*}_{de}\,(t_{n+1})}{1+\Delta t\,\Gamma\,(t_{n+1})}, \quad \beta^{*}_{de}\,(t_{n+1}) = \sqrt{\frac{3}{2}}\|\operatorname{dev}\left(\mathbf{b}'^{*}_{de}\,(t_{n+1})\right)\|.
\end{aligned} \tag{18}$$

In order to evaluate the value of the total rate of distortional deformation at time step t_{n+1}, Papes [58] defined a strongly objective estimate for the rate of deformation $\mathbf{d}$. In the present paper, we propose another strongly objective estimate for the rate of deformation $\mathbf{d}$, which is motivated by the time derivative of the relative deformation tensor $\mathbf{C}_r = \mathbf{F}_r^{\mathsf{T}}\mathbf{F}_r$ and is defined by

$$\mathbf{d}\,(t_{n+1}) = \frac{1}{2\Delta t}\left(\mathbf{I} - \mathbf{b}_r^{-1}\,(t_{n+1})\right), \quad \mathbf{b}_r\,(t_{n+1}) = \mathbf{F}_r\,(t_{n+1})\,\mathbf{F}_r^{\mathsf{T}}\,(t_{n+1})\,. \tag{19}$$

Furthermore, the estimation for the hardening variable β at time step t_{n+1} can be obtained by using the backward Euler differentiation such that

$$\beta\,(t_{n+1}) = \beta\,(t_n) + \Delta t\,\widehat{\beta}\,(\dot{\varepsilon}\,(t_{n+1})\,,\ \Gamma\,(t_{n+1})\,,\ \beta\,(t_{n+1})\,,\ \beta_{de}\,(t_{n+1}))\,. \tag{20}$$

DOI: 10.1002/cnm

For general functional forms of $\left\{\Gamma = \widehat{\Gamma}\left(\dot{\varepsilon},\, \beta,\, \beta_{de}\right),\, \dot{\beta} = \widehat{\beta}\left(\dot{\varepsilon},\, \Gamma,\, \beta,\, \beta_{de}\right)\right\}$, it is necessary to use iterative methods to find the specific values of Γ and the isotropic hardening variable β at the time step t_{n+1}. Specifically, the vector of the unknowns $\mathbf{z} = \{\Gamma\left(t_{n+1}\right),\, \beta\left(t_{n+1}\right)\}^{\mathsf{T}}$ can be obtained by solving the following set of nonlinear algebraic equations

$$\begin{aligned}
\phi_1 &= \Gamma(t_{n+1}) - \widehat{\Gamma}\left(\dot{\varepsilon}\left(t_{n+1}\right),\, \beta\left(t_{n+1}\right),\, \beta_{de}\left(t_{n+1}\right) = \frac{\beta^{*}_{de}\left(t_{n+1}\right)}{1 + \Delta t \Gamma\left(t_{n+1}\right)}\right) = 0,\\
\phi_2 &= \beta\left(t_{n+1}\right) - \beta\left(t_n\right) - \Delta t \widehat{\beta}\left(\dot{\varepsilon}\left(t_{n+1}\right),\, \Gamma\left(t_{n+1}\right),\, \beta\left(t_{n+1}\right),\, \beta_{de}\left(t_{n+1}\right) = \frac{\beta^{*}_{de}\left(t_{n+1}\right)}{1 + \Delta t \Gamma\left(t_{n+1}\right)}\right) = 0.
\end{aligned} \tag{21}$$

This system is iteratively solved by using the Newton–Raphson method with the following iterative scheme:

$$\left.\frac{\partial \boldsymbol{\phi}}{\partial \mathbf{z}}\right|_{\mathbf{z}=\mathbf{z}^i} \Delta \mathbf{z}^i + \boldsymbol{\phi}|_{\mathbf{z}=\mathbf{z}^i} = \mathbf{0}, \quad \mathbf{z}^{i+1} = \mathbf{z}^i + \Delta \mathbf{z}^i. \tag{22}$$

Finally, the spherical part of the elastic distortional deformation associated with the dissipative component, $\mathbf{b}'_{de}$, is obtained from the requirement that $\mathbf{b}'_{de}$ is a unimodular tensor, which leads to the following cubic equation

$$\left(\frac{\alpha_1}{3}\right)^3 - \frac{1}{2}\left(\operatorname{dev}\left(\mathbf{b}'_{de}\right) : \operatorname{dev}\left(\mathbf{b}'_{de}\right)\right)\left(\frac{\alpha_1}{3}\right) - \left(1 - \det\left(\operatorname{dev}\left(\mathbf{b}'_{de}\right)\right)\right) = 0. \tag{23}$$

A discussion on the solution procedure of (23) can be found in [52].

4. SPATIAL TANGENT MODULI

The consistent spatial tangent moduli, which determine the sensitivity of the developed algorithmic expressions for the stresses in terms of the change of the relative deformation gradient, play a crucial role in the FE calculation because they serve as iteration operators when the Newton–Raphson method is applied. Specifically, the spatial tangent moduli read

$$\mathsf{a}\left(t_{n+1}\right) = \frac{1}{J\left(t_{n+1}\right)} \frac{\partial \boldsymbol{\tau}\left(t_{n+1}\right)}{\partial \mathbf{F}_r} \mathbf{F}_r^{\mathsf{T}}\left(t_{n+1}\right) - \boldsymbol{\sigma}\left(t_{n+1}\right) \oplus \mathbf{I}, \tag{24}$$

where $\boldsymbol{\tau}\left(t_{n+1}\right) = J\left(t_{n+1}\right)\boldsymbol{\sigma}\left(t_{n+1}\right)$ is the Kirchhoff stress tensor and the tensor operation $\oplus$ is defined by $(\mathbf{A} \oplus \mathbf{B})_{ijkl} = A_{il}B_{jk}$. According to (7), the Cauchy stress tensor and, therefore, the Kirchhoff stress tensor are functions of the invariants of the deformation and the deviatoric part of the unimodular tensors $\{\mathbf{b}',\, \mathbf{b}'^2,\, \mathbf{b}'_{de},\, \mathbf{b}'^2_{de}\}$. However, the Cauchy stress tensor for the Rubin and Bodner model [46] (13) is a function of $\{J,\, \beta_1, \alpha_1,\, \operatorname{dev}(\mathbf{b}'),\, \operatorname{dev}(\mathbf{b}'_{de})\}$; therefore, the spatial tangent moduli are developed for the Rubin and Bodner model in this section, while the spatial tangent moduli are recorded in Appendix B for the generalized model (6). Using $(15d,g)$ and $(16a,b)$, it can be shown that the derivatives of the invariants $\{J\left(t_{n+1}\right) = J_r\left(t_{n+1}\right) J\left(t_n\right),\, \beta_1\left(t_{n+1}\right) = \mathbf{b}'\left(t_{n+1}\right) : \mathbf{I},\, \lambda_I\left(t_{n+1}\right) = \|\mathbf{m}_I\left(t_{n+1}\right)\|,\, \mathbf{m}_I\left(t_{n+1}\right) = \mathbf{F}_r\left(t_{n+1}\right)\mathbf{F}\left(t_n\right) \cdot \mathbf{M}_I\}$ and the deviatoric part of the total distortional deformation $\operatorname{dev}(\mathbf{b}')$ with respect to the relative deformation gradient are given by

$$\begin{aligned}
\frac{\partial J\left(t_{n+1}\right)}{\partial \mathbf{F}_r} \mathbf{F}_r^{\mathsf{T}}\left(t_{n+1}\right) &= J\left(t_{n+1}\right)\mathbf{I},\\
\frac{\partial \beta_1\left(t_{n+1}\right)}{\partial \mathbf{F}_r} \mathbf{F}_r^{\mathsf{T}}\left(t_{n+1}\right) &= 2\operatorname{dev}\left(\mathbf{b}'\left(t_{n+1}\right)\right),\\
\frac{\partial \lambda_I\left(t_{n+1}\right)}{\partial \mathbf{F}_r} \mathbf{F}_r^{\mathsf{T}}\left(t_{n+1}\right) &= \frac{1}{\lambda_I\left(t_{n+1}\right)} \mathbf{m}_I\left(t_{n+1}\right) \otimes \mathbf{m}_I\left(t_{n+1}\right),\\
\frac{\partial \operatorname{dev}\left(\mathbf{b}'\left(t_{n+1}\right)\right)}{\partial \mathbf{F}_r} \mathbf{F}_r^{\mathsf{T}}\left(t_{n+1}\right) &= \mathbf{b}'\left(t_{n+1}\right) \oplus \mathbf{I} + \mathbf{I} \ominus \mathbf{b}'\left(t_{n+1}\right) - \frac{2}{3}\mathbf{b}'\left(t_{n+1}\right) \otimes \mathbf{I}\\
&\quad - \frac{2}{3}\mathbf{I} \otimes \mathbf{b}'\left(t_{n+1}\right) + \frac{2}{9}\beta_1\left(t_{n+1}\right)\mathbf{I} \otimes \mathbf{I},
\end{aligned} \tag{25}$$

DOI: 10.1002/cnm

where the special tensor operation $\ominus$ is defined by $(\mathbf{A}\ominus\mathbf{B})_{ijkl} = A_{ik}B_{jl}$. Also using (23), the derivative of the trace of the elastic distortional deformation tensor associated with the dissipative part α_1 with respect to the relative deformation gradient is given by

$$\frac{\partial\alpha_1\left(t_{n+1}\right)}{\partial\mathbf{F}_r}\mathbf{F}_r^{\intercal}\left(t_{n+1}\right)=\boldsymbol{\alpha}_1\left(t_{n+1}\right),\quad \boldsymbol{\alpha}_1\left(t_{n+1}\right)=\overline{\boldsymbol{\alpha}}_1\left(t_{n+1}\right):\frac{\partial\mathrm{dev}\left(\mathbf{b}'_{de}\left(t_{n+1}\right)\right)}{\partial\mathbf{F}_r}\mathbf{F}_r^{\intercal}\left(t_{n+1}\right),$$
$$\overline{\boldsymbol{\alpha}}_1(t_{n+1})=\frac{9}{\alpha_1^2(t_{n+1})-\beta_{de}^2(t_{n+1})}\left[\frac{\alpha_1\left(t_{n+1}\right)}{3}\mathrm{dev}\left(\mathbf{b}'_{de}\left(t_{n+1}\right)\right)-\mathrm{cof}\left(\mathrm{dev}\left(\mathbf{b}'_{de}\left(t_{n+1}\right)\right)\right)\right]. \tag{26}$$

Next, it can be shown that the derivative of $\mathrm{dev}(\mathbf{b}'_{de}\left(t_{n+1}\right))$ with respect to the relative deformation gradient is given by

$$\frac{\partial\mathrm{dev}\left(\mathbf{b}'_{de}\left(t_{n+1}\right)\right)}{\partial\mathbf{F}_r}\mathbf{F}_r^{\intercal}\left(t_{n+1}\right)=\frac{1}{1+\Delta t\,\Gamma\left(t_{n+1}\right)}\left[\frac{\partial\mathrm{dev}\left(\mathbf{b}'^{*}_{de}\left(t_{n+1}\right)\right)}{\partial\mathbf{F}_r}\mathbf{F}_r^{\intercal}\left(t_{n+1}\right)\right.$$
$$\left.-\Delta t\;\mathrm{dev}\left(\mathbf{b}'_{de}\left(t_{n+1}\right)\right)\otimes\boldsymbol{\Gamma}\left(t_{n+1}\right)\right], \tag{27}$$

where the expression for the derivative of $\mathrm{dev}(\mathbf{b}'^{*}_{de}\left(t_{n+1}\right))$ is defined in a similar manner to $(25d)$ by replacing $\mathbf{b}'\left(t_{n+1}\right)$ with $\mathbf{b}'^{*}_{de}\left(t_{n+1}\right)$. Now, taking the derivative of the two implicit equations for $\{\Gamma,\beta\}$ (21) and using Equations $(3a)$, $(18c)$, and $(19a)$, the tensor $\boldsymbol{\Gamma}\left(t_{n+1}\right)$ in (27) reads

$$\boldsymbol{\Gamma}\left(t_{n+1}\right)=\frac{2}{3\Delta t\,\dot{\varepsilon}\left(t_{n+1}\right)}\frac{d_1\left(t_{n+1}\right)}{d_0\left(t_{n+1}\right)}\mathbf{b}_r^{-1}\left(t_{n+1}\right)\mathrm{dev}\left(\mathbf{d}\left(t_{n+1}\right)\right)$$
$$+\frac{d_2\left(t_{n+1}\right)}{d_0\left(t_{n+1}\right)}\left[\frac{3}{\beta^{*}_{de}\left(t_{n+1}\right)}\mathrm{dev}\left(\mathbf{b}'^{*}_{de}\left(t_{n+1}\right)\right)\mathbf{b}'^{*}_{de}\left(t_{n+1}\right)-\frac{2}{3}\beta^{*}_{de}\left(t_{n+1}\right)\mathbf{I}\right], \tag{28}$$

where the coefficients $\{d_0\left(t_{n+1}\right),\,d_1\left(t_{n+1}\right),\,d_2\left(t_{n+1}\right)\}$ are given in Appendix C. Finally, multiplying the stress expression (13) by J, substituting the result into (24), and using (25) and (26), the spatial tangent moduli read

$$\mathsf{a}\left(t_{n+1}\right)=m_1\mu\left(t_{n+1}\right)\mathbf{I}\otimes\mathbf{I}+m_2\frac{\mu\left(t_{n+1}\right)}{J\left(t_{n+1}\right)}\frac{\partial\mathrm{dev}\left(\mathbf{b}'\left(t_{n+1}\right)\right)}{\partial\mathbf{F}_r}\mathbf{F}_r^{\intercal}\left(t_{n+1}\right)$$
$$+\frac{\mu\left(t_{n+1}\right)}{2J\left(t_{n+1}\right)}\sum_{I=1}^{N_{\mathrm{fib.}}}\frac{1}{\lambda_I\left(t_{n+1}\right)}\frac{d}{d\lambda_I}\left(\frac{d\,g_3/d\lambda_I}{\lambda_I\left(t_{n+1}\right)}\right)\overline{\mathbf{m}}_I\left(t_{n+1}\right)\otimes\overline{\mathbf{m}}_I\left(t_{n+1}\right)$$
$$+\frac{\mu\left(t_{n+1}\right)}{2J\left(t_{n+1}\right)}\sum_{I=1}^{N_{\mathrm{fib.}}}\frac{d\,g_3/d\lambda_I}{\lambda_I\left(t_{n+1}\right)}\left(\overline{\mathbf{m}}_I\left(t_{n+1}\right)\oplus\mathbf{I}+\mathbf{I}\ominus\overline{\mathbf{m}}_I\left(t_{n+1}\right)\right)$$
$$+m_5\frac{\mu\left(t_{n+1}\right)}{J\left(t_{n+1}\right)}\frac{\partial\mathrm{dev}\left(\mathbf{b}'_{de}\left(t_{n+1}\right)\right)}{\partial\mathbf{F}_r}\mathbf{F}_r^{\intercal}\left(t_{n+1}\right)$$
$$+\boldsymbol{\sigma}\left(t_{n+1}\right)\otimes\mathbf{g}\left(t_{n+1}\right)-\boldsymbol{\sigma}\left(t_{n+1}\right)\oplus\mathbf{I}, \tag{29}$$

where $\overline{\mathbf{m}}_I\left(t_{n+1}\right)$ is the current structural tensor of the I'th fiber family defined by

$$\overline{\mathbf{m}}_I\left(t_{n+1}\right)=\mathbf{m}_I\left(t_{n+1}\right)\otimes\mathbf{m}_I\left(t_{n+1}\right), \tag{30}$$

and $\{\mu\left(t_{n+1}\right),\,\mathbf{g}\left(t_{n+1}\right)\}$ are, respectively, defined by

$$\mu\left(t_{n+1}\right)=\mu_0 e^{q\,g\left(t_{n+1}\right)},$$
$$\mathbf{g}\left(t_{n+1}\right)=q\frac{\partial g\left(t_{n+1}\right)}{\partial\mathbf{F}_r}\mathbf{F}_r^{\intercal}\left(t_{n+1}\right)=2qm_1\left(J\left(t_{n+1}\right)-1\right)+2qm_2\mathrm{dev}\left(\mathbf{b}'\left(t_{n+1}\right)\right)$$
$$+2qm_3\sum_{I=1}^{N_{\mathrm{fib.}}}\frac{\langle\lambda_I\left(t_{n+1}\right)-1\rangle^{2m_4-1}}{\lambda_I\left(t_{n+1}\right)}\overline{\mathbf{m}}_I\left(t_{n+1}\right)+qm_5\boldsymbol{\alpha}_1. \tag{31}$$

DOI: 10.1002/cnm

5. FINITE ELEMENT FORMULATION

A new mixed FE formulation, particularly suitable for viscoplastic material models involving evolution equations of the measures of deformation, is developed here for the numerical study of soft tissues. It turned out that the reference configuration of the body in the present development became irrelevant, and all calculations are carried out on the deformed configurations at time t_n and t_{n+1}. Generally speaking, the mixed formulation for nearly incompressible materials can be derived by using the Hu–Washizu functional, where the independent variables are the deformation gradient, an assumed dilatation measure, and an assumed hydrostatic pressure. In particular, the Hu–Washizu functional can be written as

$$\Pi\left(\tilde{\mathbf{F}},\, \overline{J}_r,\, \overline{p}\right) = \int_{\Omega_{t_n}} \left[\frac{1}{J\,(t_n)} W\left(\tilde{\mathbf{F}}\right) + \overline{p}\left(J_r - \overline{J}_r\right)\right] d\Omega_n - \Pi^{ext}, \tag{32}$$

where Ω_n is the element domain at time t_n, Π^{ext} is the potential energy due to external forces, $\overline{J}_r$ is a scalar related to the relative volumetric dilatation, $\overline{p}$ is a scalar related to hydrostatic pressure (spherical part of stress), and $\tilde{\mathbf{F}}$ is the modified deformation gradient that can be multiplicatively decomposed into a modified relative deformation gradient and a modified deformation gradient at time t_n such that

$$\tilde{\mathbf{F}} = \tilde{\mathbf{F}}_r \tilde{\mathbf{F}}\,(t_n)\,, \quad \tilde{\mathbf{F}}_r = \left(\frac{\overline{J}_r}{J_r}\right)^{1/3} \mathbf{F}_r, \quad \tilde{\mathbf{F}}\,(t_n) = \left(\frac{\overline{J}\,(t_n)}{J\,(t_n)}\right)^{1/3} \mathbf{F}\,(t_n)\,. \tag{33}$$

The variation of the functional (32) with respect to the different fields yields the following three equations

$$\begin{aligned}
\delta_{\mathbf{F}_r}\Pi &= \int_{\Omega} \tilde{\tilde{\boldsymbol{\sigma}}} : \delta\mathbf{h}\, d\Omega - \delta\Pi^{ext}, \quad \tilde{\tilde{\boldsymbol{\sigma}}} = \frac{\overline{J}}{J}\mathrm{dev}\,(\tilde{\boldsymbol{\sigma}}\,) + \overline{p}\mathbf{I}, \quad \delta\mathbf{h} = \frac{\partial\delta\mathbf{u}}{\partial\mathbf{x}}, \\
\delta_{\overline{p}}\Pi &= \int_{\Omega_n} \left(J_r - \overline{J}_r\right)\delta\overline{p}\, d\Omega_n, \\
\delta_{\overline{J}_r}\Pi &= \int_{\Omega_n} \left(\frac{\overline{J}\,(t_n)}{J\,(t_n)}\tilde{p} - \overline{p}\right)\delta\overline{J}_r\, d\Omega_n, \quad \tilde{p} = \frac{1}{3}\tilde{\boldsymbol{\sigma}} : \mathbf{I},
\end{aligned} \tag{34}$$

where Ω is the deformed element domain at time t_{n+1}, $\tilde{\boldsymbol{\sigma}}$ is evaluated according to (7) (or according to (13) for the Rubin–Bodner model) where $\{\tilde{\mathbf{F}}_r,\, \tilde{\mathbf{F}}\,(t_n)\}$ are used instead of $\{\mathbf{F}_r,\, \mathbf{F}\,(t_n)\}$, and $\delta\mathbf{u}$ is the virtual displacement field. Now, assuming that the variables $\{\overline{J}_r,\, \overline{p}\}$ are constants at the element domain, the variational equations (34*b*,*c*) yield the following explicit equations for the determination of the fields $\{\overline{J}_r,\, \overline{p}\}$, respectively,

$$\overline{J}_r = \frac{1}{\Omega_n}\int_{\Omega_n} J_r\, d\Omega_n, \quad \overline{p} = \frac{1}{\Omega_n}\int_{\Omega_n} \frac{\overline{J}\,(t_n)}{J\,(t_n)}\tilde{p}\, d\Omega_n. \tag{35}$$

According to (35), the variable $\overline{J}_r$ can be interpreted as the ratio between the element volume at time t_{n+1} and t_n, while the variable $\overline{p}$ is the average hydrostatic pressure within the element domain. Also, the linearization of the variation of the functional (32) is given by

$$\begin{aligned}
\Delta\delta\Pi = \int_{\Omega} \Bigg[& \delta\mathbf{h} : \left(\tilde{\mathbf{a}}_{uu} : \Delta\mathbf{h} + \tilde{\mathbf{a}}_{u\overline{J}_r}\frac{\Delta\overline{J}_r}{\overline{J}_r} + \mathbf{I}\Delta\overline{p}\right) \\
& + \frac{\delta\overline{J}_r}{\overline{J}_r}\left(\tilde{\mathbf{a}}_{\overline{J}_r u} : \Delta\mathbf{h} + \tilde{a}_{\overline{J}_r\overline{J}_r}\frac{\Delta\overline{J}_r}{\overline{J}_r} - \frac{\overline{J}_r}{J_r}\Delta\overline{p}\right) \\
& + \delta\overline{p}\left(\mathbf{I} : \Delta\mathbf{h} - \frac{\overline{J}_r}{J_r}\frac{\Delta\overline{J}_r}{\overline{J}_r}\right)\Bigg]\, d\Omega\,,
\end{aligned} \tag{36}$$

DOI: 10.1002/cnm

where the tensor $\Delta\mathbf{h}$ is defined in a similar manner to $\delta\mathbf{h}$ in (34c) by replacing the virtual displacement field $\delta\mathbf{u}$ with the incremental displacement field $\Delta\mathbf{u}$. The fourth-order tensor $\tilde{\mathsf{a}}_{uu}$, the second-order tensors $\{\tilde{\mathbf{a}}_{u\overline{J}_r}, \tilde{\mathbf{a}}_{\overline{J}_r u}\}$, and the scalar $\tilde{a}_{\overline{J}_r\,\overline{J}_r}$ are defined by

$$\begin{aligned}
\tilde{\mathsf{a}}_{uu} &= \left(\mathbb{I} - \frac{1}{3}\mathbf{I}\otimes\mathbf{I}\right) : \frac{\overline{J}}{J}\tilde{\mathsf{a}} : \left(\mathbb{I} - \frac{1}{3}\mathbf{I}\otimes\mathbf{I}\right) - \frac{1}{3}\left(\operatorname{dev}\left(\tilde{\bar{\boldsymbol{\sigma}}}\right)\otimes\mathbf{I} + \mathbf{I}\otimes\operatorname{dev}\left(\tilde{\bar{\boldsymbol{\sigma}}}\right)\right) \\
&\quad + \left(\frac{\overline{J}}{J}\tilde{p} - \overline{p}\right)\mathbf{I}\oplus\mathbf{I} + \left(\overline{p} - \frac{1}{3}\frac{\overline{J}}{J}\tilde{p}\right)\mathbf{I}\otimes\mathbf{I}, \\
\tilde{\mathbf{a}}_{u\overline{J}_r} &= \frac{1}{3}\left(\mathbb{I} - \frac{1}{3}\mathbf{I}\otimes\mathbf{I}\right) : \frac{\overline{J}}{J}\tilde{\mathsf{a}} : \mathbf{I} + \frac{1}{3}\operatorname{dev}\left(\tilde{\bar{\boldsymbol{\sigma}}}\right), \\
\tilde{\mathbf{a}}_{\overline{J}_r u} &= \frac{1}{3}\mathbf{I} : \frac{\overline{J}}{J}\tilde{\mathsf{a}} : \left(\mathbb{I} - \frac{1}{3}\mathbf{I}\otimes\mathbf{I}\right) + \frac{1}{3}\operatorname{dev}\left(\tilde{\bar{\boldsymbol{\sigma}}}\right), \\
\tilde{a}_{\overline{J}_r\,\overline{J}_r} &= \frac{1}{9}\mathbf{I} : \frac{\overline{J}}{J}\tilde{\mathsf{a}} : \mathbf{I} - \frac{2}{3}\frac{\overline{J}}{J}\tilde{p},
\end{aligned} \tag{37}$$

where the fourth-order tensor $\tilde{\mathsf{a}}$ in (37) is evaluated according to (B.1) in Appendix B for the generalized model or according to (29) for the Rubin Bodner model, where $\{\mathbf{F}_r,\ \mathbf{F}(t_n)\}$ are replaced by $\{\tilde{\mathbf{F}}_r,\ \tilde{\mathbf{F}}(t_n)\}$.

The ansatz spaces of the different fields have to be balanced in order to obtain a robust and stable discretization that is based on the Hu–Washizu functional (32). Therefore, a trilinear interpolation will be applied for the displacement field and a constant interpolation for the assumed dilatation and pressure terms. Specifically, the deformed configurations at time t_n and t_{n+1} are interpolated, respectively, as follows

$$\mathbf{x}(t_n) = \sum_{I=1}^{N_{en}} N^I \widehat{\mathbf{x}}_I(t_n), \quad \mathbf{x}(t_{n+1}) = \sum_{I=1}^{N_{en}} N^I \widehat{\mathbf{x}}_I(t_{n+1}), \tag{38}$$

where N^I represents the ansatz functions, N_{en} is the number of nodes per element, and $\{\widehat{\mathbf{x}}_I(t_n), \widehat{\mathbf{x}}_I(t_{n+1})\}$ are the nodal positions of the configurations at time t_n and t_{n+1}, respectively. Because the incremental displacements are given by $\Delta\mathbf{u} = \mathbf{x}(t_{n+1}) - \mathbf{x}(t_n)$, a trilinear interpolation is also used for the incremental displacement field such that

$$\Delta\mathbf{u} = \sum_{I=1}^{N_{en}} N^I \Delta\widehat{\mathbf{u}}_I, \quad \Delta\widehat{\mathbf{u}}_I = \widehat{\mathbf{x}}_I(t_{n+1}) - \widehat{\mathbf{x}}_I(t_n), \tag{39}$$

and, therefore, the relative deformation gradient is obtained by

$$\mathbf{F}_r = \left(\mathbf{I} - \sum_{I=1}^{N_{en}} \Delta\widehat{\mathbf{u}}_I \otimes \operatorname{grad}\left(N^I\right)\right)^{-1}, \quad \operatorname{grad}\left(N^I\right) = \frac{\partial N^I}{\partial\mathbf{x}}. \tag{40}$$

For developing the element residua and element tangent stiffness matrix, the matrix notation is used. It is worth noting that for the matrix notation, vectors and second-order tensors become vectors (indicated by underline) and fourth-order tensors become second-order matrices (indicated by double underline). Thus, the tensors $\delta\mathbf{h}$ and $\Delta\mathbf{h}$ can, respectively, be written as follows

$$\delta\underline{\mathbf{h}} = \underline{\underline{\mathbb{B}}}\,\delta\underline{\mathbf{d}}_u, \quad \Delta\underline{\mathbf{h}} = \underline{\underline{\mathbb{B}}}\,\Delta\underline{\mathbf{d}}_u, \tag{41}$$

where $\delta\underline{\mathbf{d}}_u$ and $\Delta\underline{\mathbf{d}}_u$ are the virtual and incremental nodal displacement vectors, respectively, and $\underline{\underline{\mathbb{B}}}$ is the standard B-matrix for finite deformation, which consists of the derivatives of the ansatz functions with respect to the deformed configuration at time t_{n+1}. Now, the residual forces defined as the difference between the external nodal forces (due to external forces) and the internal nodal forces (due to the constitutive equations) are obtained by substituting (41) into (33a) such that

DOI: 10.1002/cnm

$$\widehat{\underline{\mathbf{r}}} = \widehat{\underline{\mathbf{f}}}^{\text{ext.}} - \widehat{\underline{\mathbf{f}}}^{\text{int.}}, \quad \widehat{\underline{\mathbf{f}}}^{\text{int.}} = \int_{\Omega} \mathbb{B}^{\mathsf{T}} \tilde{\underline{\boldsymbol{\sigma}}}\, d\Omega, \tag{42}$$

and the stiffness matrix is obtained by substituting (41) into (35), using the fact that the assumed dilatation and pressure fields are constant within the element region and writing these results in a matrix form as follows

$$\Delta\delta\Pi = \begin{bmatrix} \delta\underline{\mathbf{d}}_u \\ \delta\overline{J}_r/\overline{J}_r \\ \delta\overline{p} \end{bmatrix}^{\mathsf{T}} \begin{bmatrix} \underline{\underline{\mathbf{K}}}_{uu} & \underline{\mathbf{K}}_{u\overline{J}_r} & \underline{\mathbf{K}}_{u\overline{p}} \\ \underline{\mathbf{K}}_{\overline{J}_r u} & K_{\overline{J}_r\overline{J}_r} & -K_{\overline{J}_r\overline{p}} \\ \underline{\mathbf{K}}_{\overline{p}u} & -K_{\overline{p}\overline{J}_r} & 0 \end{bmatrix} \begin{bmatrix} \Delta\underline{\mathbf{d}}_u \\ \Delta\overline{J}_r/\overline{J}_r \\ \Delta\overline{p} \end{bmatrix}, \tag{43}$$

where the submatrix $\underline{\underline{\mathbf{K}}}_{uu}$, the vectors $\{\underline{\mathbf{K}}_{u\overline{J}_r}\, \underline{\mathbf{K}}_{up}\, \underline{\mathbf{K}}_{\overline{J}_r u},\, \underline{\mathbf{K}}_{\overline{p}u}\}$, and the scalars $\left\{K_{\overline{J}_r\overline{J}_r},\, K_{\overline{J}_r p},\, K_{\overline{p}\overline{J}_r}\right\}$ are given by

$$\begin{aligned} \underline{\underline{\mathbf{K}}}_{uu} &= \int_{\Omega} \underline{\underline{\mathbb{B}}}^{\mathsf{T}}\, \underline{\underline{\tilde{\mathbf{a}}}}_{uu}\, \underline{\underline{\mathbb{B}}}\, d\Omega, \quad \underline{\mathbf{K}}_{u\overline{J}_r} = \int_{\Omega} \underline{\underline{\mathbb{B}}}^{\mathsf{T}} \underline{\tilde{\mathbf{a}}}_{u\overline{J}_r}\, d\Omega, \quad \underline{\mathbf{K}}_{u\overline{p}} = \underline{\mathbf{K}}^{\mathsf{T}}_{\overline{p}u} = \int_{\Omega} \underline{\underline{\mathbb{B}}}^{\mathsf{T}} \underline{\mathbf{I}}\, d\Omega \\ \underline{\mathbf{K}}_{\overline{J}_r u} &= \int_{\Omega} \underline{\mathbf{a}}_{\overline{J}_r u} \underline{\underline{\mathbb{B}}}\, d\Omega, \quad K_{\overline{J}_r\overline{J}_r} = \int_{\Omega} a_{\overline{J}_r\overline{J}_r}\, d\Omega, \quad K_{\overline{J}_r\overline{p}} = K_{\overline{p}\overline{J}_r} = \int_{\Omega} \frac{\overline{J}}{J}\, d\Omega. \end{aligned} \tag{44}$$

Because the quantities $\{\overline{J}_r,\, \overline{p}\}$ are not assembled over all elements but are determined at the element level, it is advantageous to perform a static condensation and eliminate the quantities $\{\overline{J}_r,\, \overline{p}\}$. Specifically, the tangent stiffness matrix then reads

$$\underline{\underline{\mathbf{K}}} = \underline{\underline{\mathbf{K}}}_{uu} + \frac{1}{K_{\overline{p}\overline{J}_r}} \underline{\mathbf{K}}_{\overline{p}u} \underline{\mathbf{K}}_{u\overline{J}_r} + \frac{1}{K_{\overline{J}_r\overline{p}}} \underline{\mathbf{K}}_{\overline{J}_r u} \underline{\mathbf{K}}_{u\overline{p}} + \frac{K_{\overline{J}_r\overline{J}_r}}{K_{\overline{p}\overline{J}_r} K_{\overline{J}_r\overline{p}}} \underline{\mathbf{K}}_{\overline{p}u} \underline{\mathbf{K}}_{u\overline{p}}. \tag{45}$$

The developed mixed FE was implemented into the commercial FE package Abaqus [62] (Dassault Systèmes, Providence, RI, USA) within the user subroutine UEL. In particular, Abaqus calls the UEL subroutine with a guess for the nodal displacements of the element, and the UEL subroutine provides Abaqus with the element residua, RHS, (42) and the element tangent stiffness matrix, AMATRX, (45) of the governing equations.

6. NUMERICAL VERIFICATIONS

The newly developed mixed FE formulation and its implementation in the commercial FE software Abaqus [62] are verified by considering a number of standard numerical tests including patch test, rate of convergence test, and objectivity test. For these simulations, a set of material parameters determined by Rubin and Bodner [46] is used. In particular, these specific parameters are based on experimental work by Har-Shai *et al.* [63], where uniaxial tension tests on strips of excised human skin were conducted, allowing to determine the stress–strain relationship under cyclic loading at varying strain rates.

6.1. Patch test

The patch test is considered as a fundamental test in FE technology and has been used for over five decades as a condition for convergence and as a verification tool for FE algorithms (e.g., Taylor *et al.* [64], Babuska and Narasimhan [65], and Zienkiewicz and Taylor [66]). Different variants of the patch test have been suggested by different research works, and the force version of the patch test has been applied in this study. To this end, a cube with edge length $a = 20.0\,\text{mm}$ and meshed by seven distorted elements is considered (Figure 1a). The reference locations $\mathbf{X}_I$ $(I = 1, \ldots, 16)$ of the nodes of the seven elements in Figure 1a are specified by

DOI: 10.1002/cnm

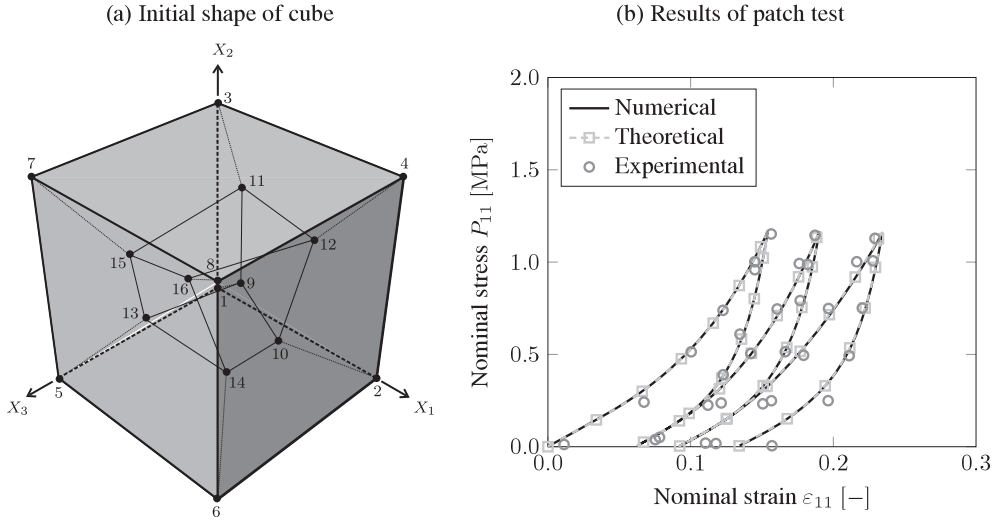

Figure 1. Patch test for numerical verification of the constitutive equations. (a) Geometric representation of a cube discretized by seven initially distorted hexahedral elements. (b) Results of the patch test. Comparison between theoretical and numerical uniaxial nominal stress P_{11}. Fair agreement between experimental data and the model prediction is observed for the material parameters presented by [46].

$$\begin{aligned}
&\mathbf{X}_1 = \mathbf{0}, \quad \mathbf{X}_2 = a\mathbf{e}_1, \quad \mathbf{X}_3 = a\mathbf{e}_2, \quad \mathbf{X}_4 = a\mathbf{e}_1 + a\mathbf{e}_2,\\
&\mathbf{X}_5 = a\mathbf{e}_3, \quad \mathbf{X}_6 = a\mathbf{e}_1 + a\mathbf{e}_3, \quad \mathbf{X}_7 = a\mathbf{e}_2 + a\mathbf{e}_3, \quad \mathbf{X}_8 = a\mathbf{e}_1 + a\mathbf{e}_2 + a\mathbf{e}_3,\\
&\mathbf{X}_9 = 0.35a\mathbf{e}_1 + 0.30a\mathbf{e}_2 + 0.20a\mathbf{e}_3, \quad \mathbf{X}_{10} = 0.80a\mathbf{e}_1 + 0.35a\mathbf{e}_2 + 0.45a\mathbf{e}_3,\\
&\mathbf{X}_{11} = 0.30a\mathbf{e}_1 + 0.75a\mathbf{e}_2 + 0.15a\mathbf{e}_3, \quad \mathbf{X}_{12} = 0.75a\mathbf{e}_1 + 0.70a\mathbf{e}_2 + 0.20a\mathbf{e}_3,\\
&\mathbf{X}_{13} = 0.20a\mathbf{e}_1 + 0.25a\mathbf{e}_2 + 0.65a\mathbf{e}_3, \quad \mathbf{X}_{14} = 0.75a\mathbf{e}_1 + 0.30a\mathbf{e}_2 + 0.70a\mathbf{e}_3,\\
&\mathbf{X}_{15} = 0.25a\mathbf{e}_1 + 0.65a\mathbf{e}_2 + 0.75a\mathbf{e}_3, \quad \mathbf{X}_{16} = 0.65a\mathbf{e}_1 + 0.75a\mathbf{e}_2 + 0.80a\mathbf{e}_3.
\end{aligned} \tag{46}$$

Also, the cube was subjected to axial stretch in the $\mathbf{e}_1$ direction, which causes a uniaxial stress in the $\mathbf{e}_1$ direction. In the present example, three subsequent loading and unloading cycles of axial stretch with different rates were prescribed similar to the uniaxial tests performed by Har-Shai *et al.* [63].

For calculating the theoretical uniaxial stress, the relative deformation gradient $\mathbf{F}_r$ that is evaluated at the end of a typical time step is given by

$$\mathbf{F}_r\left(t_{n+1}\right) = \frac{\lambda_1\left(t_{n+1}\right)}{\lambda_1\left(t_n\right)}\mathbf{e}_1 \otimes \mathbf{e}_1 + \frac{\lambda_2\left(t_{n+1}\right)}{\lambda_2\left(t_n\right)}\mathbf{e}_2 \otimes \mathbf{e}_2 + \frac{\lambda_3\left(t_{n+1}\right)}{\lambda_3\left(t_n\right)}\mathbf{e}_3 \otimes \mathbf{e}_3, \tag{47}$$

where $\{\lambda_i\left(t_n\right), \lambda_i\left(t_{n+1}\right)\}$ are the stretches at time steps t_n and t_{n+1}, respectively. The lateral stretches $\{\lambda_2\left(t_{n+1}\right), \lambda_3\left(t_{n+1}\right)\}$ are determined by iteration to satisfy the boundary condition of vanishing lateral stress

$$\boldsymbol{\sigma}\colon(\mathbf{e}_2 \otimes \mathbf{e}_2) = 0, \quad \boldsymbol{\sigma}\colon(\mathbf{e}_3 \otimes \mathbf{e}_3) = 0, \tag{48}$$

while the resulting axial stress is determined by Equation (13).

The numerical uniaxial Piola–Kirchhoff stress obtained by the FE solution and its theoretical counterpart are plotted in Figure 1b. It can be seen that both solutions coincide, which indicates that the derived FE formulation satisfies the patch test. Furthermore, a comparison with the experimental data used to identify the material parameters presented by Rubin and Bodner [46] is shown in Figure 1b. The generally observed agreement between experimental data and numerical prediction is a demonstration of the capability of this specific elastic–viscoplastic model to provide a fairly accurate representation of facial soft tissue response.

DOI: 10.1002/cnm

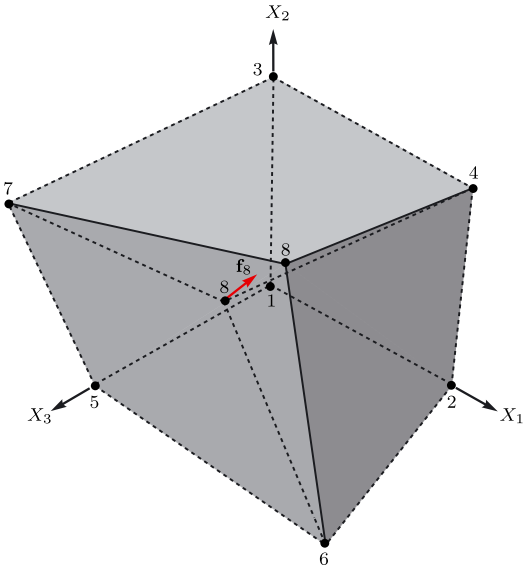

$$\mathbf{X}_1 = \mathbf{0}, \quad \mathbf{X}_2 = a\mathbf{e}_1, \quad \mathbf{X}_3 = a\mathbf{e}_2,$$

$$\mathbf{X}_4 = a\mathbf{e}_1 + a\mathbf{e}_2, \quad \mathbf{X}_5 = a\mathbf{e}_3,$$

$$\mathbf{X}_6 = 1.15a\mathbf{e}_1 - 1.15a\mathbf{e}_2 + 0.9a\mathbf{e}_3,$$

$$\mathbf{X}_7 = -a\mathbf{e}_1 + 0.9a\mathbf{e}_2 + 1.25a\mathbf{e}_3,$$

$$\mathbf{X}_8 = 1.25a\mathbf{e}_1 + 1.25a\mathbf{e}_2 + 1.5a\mathbf{e}_3.$$

Figure 2. Representation of the cube considered for the convergence test and the nodal position of the eight mesh nodes. Node #8 is subjected to a nodal force vector $\mathbf{f}_8 = \overline{f}_8\,(\mathbf{e}_1 + \mathbf{e}_2 - \mathbf{e}_3)$, with $\overline{f}_8 = 0.05\,\text{N}$.

Table I. Convergence rate of element formulation in terms of development of residual force per iteration for all four increments of $\Delta t = 0.25$.

	Step #1	Step #2	Step #3	Step #4
Iteration #1	0.10000000E+01	0.12733532E−01	0.40889563E−01	0.40196800E−01
Iteration #2	0.87260426E−01	0.20965581E−03	0.17495670E−02	0.26096952E−02
Iteration #3	0.49335789E−03	0.11649721E−06	0.94714269E−05	0.20913626E−04
Iteration #4	0.12882890E−05	0.33258373E−11	0.33819576E−09	0.15121905E−08
Iteration #5	0.69087549E−11			0.31721042E−12

6.2. Rate of convergence

The objective of the rate of convergence test is to verify that the derived spatial tangent moduli (29) ensure quadratic convergence at each equilibrium iteration. To this end, an initially distorted element is subjected to a nodal force while the remaining nodes are fixed. Figure 2 provides a geometric representation of the cube at both the reference (dashed lines) and deformed (solid lines) configurations, as well as the specific nodal position of the mesh points (with $a = 1.0\,\text{mm}$). In the simulation presented here, node #8 is subjected to $\mathbf{f}_8 = \overline{f}_8\,(\mathbf{e}_1 + \mathbf{e}_2 - \mathbf{e}_3)$, with $\overline{f}_8 = 0.05\,\text{N}$.

The rate of convergence is expressed in terms of the nodal residual force and is calculated based on a fixed incremental time step of $\Delta t = 0.25\,\text{s}$ with a total simulation time of $t = 1.0\,\text{s}$. The residual force after each iteration for all four increments is given in Table I, which demonstrates quadratic convergence through the apparent decay of the order of magnitude of the residual force.

6.3. Objectivity test

The principle of material invariance is a fundamental prerequisite in continuum mechanics and postulates that the constitutive response remains independent of the observer. Hence, the objective of this test is to confirm that the presented integration scheme in Section 3 properly integrates the constitutive evolution equations under SRBM.

Specifically, an element is encapsulated by a network of slide plane elements, allowing us to superpose a uniaxial stretch and rotation on the cube simultaneously (Figure 3a). Boundary conditions are applied to node #1, at which translational degrees of freedom are fixed and an angular velocity given by $\boldsymbol{\omega} = \bar{\omega}\,(\mathbf{e}_1 + \mathbf{e}_2 + \mathbf{e}_3)$ is prescribed. The cube is subjected to six steps of loading

DOI: 10.1002/cnm

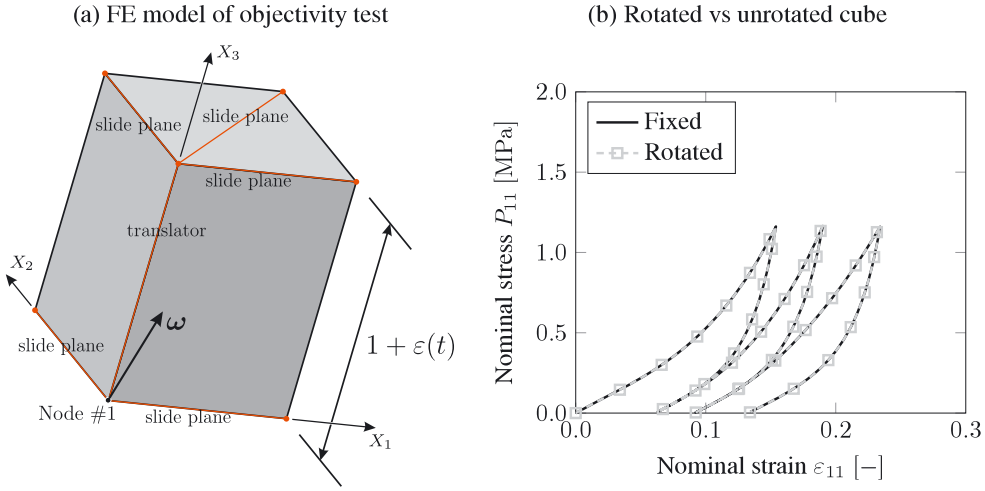

Figure 3. (a) Finite element (FE) model for the objectivity test. Translational degrees of freedom at node #1 are fixed, while a rotation is prescribed and the translator element is simultaneously stretched, which induces a uniaxial stress state in the cube. (b) Comparison between numerical results for the fixed and rotated cubes under cyclic, uniaxial stress.

Table II. Loading profile in terms of time steps, strain rates, and angular velocities for validating the strong incremental objectivity of the presented numerical integration.

Step	Time interval (s)	Strain rate $\dot{\varepsilon}\,(t)$ (Hz)	Angular velocity $\tilde{\omega}$ (rad/s)
1	15.4	$+1.0 \cdot 10^{-2}$	$3.925972 \cdot 10^{-2}$
2	9.1	$-1.0 \cdot 10^{-2}$	$6.643954 \cdot 10^{-2}$
3	50.8	$+2.5 \cdot 10^{-3}$	$1.190157 \cdot 10^{-2}$
4	39.2	$-2.5 \cdot 10^{-3}$	$1.542346 \cdot 10^{-2}$
5	284.0	$+5.0 \cdot 10^{-4}$	$2.128872 \cdot 10^{-2}$
6	200.0	$-5.0 \cdot 10^{-4}$	$0.302300 \cdot 10^{-2}$

and unloading at different strain rates, similar to the experiments by Har-Shai [63]. Additionally, a rotation angle of 60° around the direction of $\boldsymbol{\omega}$ is prescribed at each step.

The applied loading profile for the recomputation of the experiments by Har-Shai [63] is summarized in Table II. The angular velocity applied to node #1 is given in terms of $\tilde{\omega} = \bar{\omega}/t$, with $\bar{\omega} = \alpha/\sqrt{3}$, for arbitrary rotation angle α (e.g., $\alpha = 60°$) around $\boldsymbol{\omega}$ and step time t.

Figure 3b shows a comparison between the rotated cyclic test and the same example without a prescribed rotation. It can be seen that both curves coincide, which leads to the conclusion that the integration scheme is objective.

7. PARAMETER IDENTIFICATION OF FACIAL SKIN TISSUE

In this section, a set of model parameters is derived from mechanical experiments on human facial skin using the suction method. In comparison with material parameters presented by Rubin and Bodner [46] and Mazza *et al.* [16], the measurements considered here describe a more realistic state of strain within the tissue as for the uniaxial tests by Har-Shai [63] and allow for the identification of an improved set of model parameters. Moreover, the parameter optimization procedure presented here can be considered as a challenging example of the implementation's applicability.

Several different non-invasive testing methods have been used to investigate the mechanical properties of skin including suction [67–71], indentation [72, 73], and *in situ* tensioning devices [74–76]. Specifically, suction devices such as the commercially available Cutometer MPA 580 (Courage and Khazaka Electronic GmbH, Köln, Germany) and the Aspiration device (developed at ETH Zürich

DOI: 10.1002/cnm

[9, 23, 41]) have been shown to provide a reliable and repeatable testing method for the characterization of individual tissue layers. Depending on the probe aperture diameter, different tissue layers are addressed, which impacts the penetration depth and hence allows us to determine the properties of individual tissues through solving an inverse FE problem [41]. In the present study, we focus on the most superficial layer of the face, that is, skin tissue, and therefore, the Cutometer device with a probe aperture diameter of 2 mm is used. However, in order to determine material model parameters valid for deeper tissue layers in the face, such as the superficial muscular aponeurotic system (SMAS), superficial and deep fat, more experimental data are required that should be obtained using a suction device with a bigger probe aperture (e.g., the Aspiration device with an 8-mm probe).

In the following, the Cutometer measurements are presented, a set of model parameters for facial skin is determined, and a sensitivity analysis on the underlying inverse FE model (including boundary conditions, model dimensions, and material parameters) is shown.

7.1. Cutometer measurements on facial skin

The Cutometer device is based on the suction method, allowing for a quantitative measurement of tissue response. Inside the Cutometer device, a negative pressure is created, causing skin tissue to be sucked into the aperture of the probe. The resulting tissue deformation is captured through an optical system that evaluates the penetration depth for the corresponding loading state. In the series of measurements presented here, two measurement protocols with different loading profiles were defined in order to assess different tissue properties. In the first measurement protocol, a negative pressure is applied at once and held constant for 20 s, thus addressing the following: (i) instantaneous tissue response and (ii) the time-dependent creep response. In the second protocol, a linearly varying negative pressure at a constant pressure rate is prescribed in order to load and unload the tissue subsequently. This second experiment allows us to determine the impact of the following: (i) strain-rate-driven hardening; (ii) strain-rate-driven plastification; and (iii) material recovery during unloading.

For both loading profiles, three different levels of loading were considered. Pressure levels of 300, 400, and 500 mbar were applied in the first measurement protocol and pressure rates of 10, 15, and 20 mbar/s for the second. Each of the six measurements was repeated for at least four times in order to ensure repeatability. Measurements were performed on a male subject aged 29 years, and measurement position was chosen based on experiments presented by Barbarino *et al.* [41] to be in between the zygomatic and nasolabial regions because these were found to be closest to the facial average. Figures 4 and 5 show the results of the measurements, where the gray lines represent the individual measurements and the black lines represent the three averages for each sequence of measurements at a different pressure level. Specifically, Figure 4 shows the measurement series for

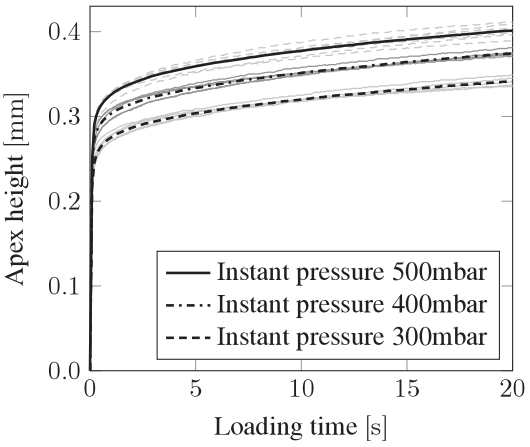

Figure 4. Experimental data from Cutometer measurements for the case of instant loading with four to six repetitions per pressure level (gray curves) and average curves for each pressure level (black curves).

DOI: 10.1002/cnm

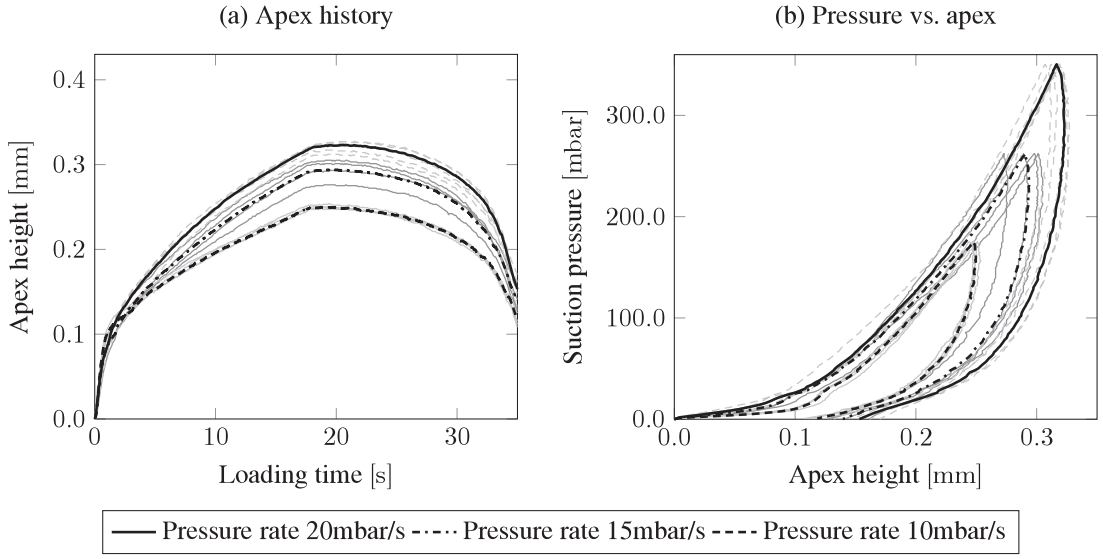

Figure 5. Experimental data from Cutometer measurements for the case of linear loading and unloading. Gray curves represent four to six individual measurements per pressure rate, and black curves are averaged data over each pressure rate. (a) Apex height over measurement time . (b) Suction pressure over apex height.

the case of instant loading. Figure 5 shows the experimental data for the case of linear loading and unloading in two different ways, where the apex height history is plotted in Figure 5a and the applied suction pressure versus the apex height is plotted in Figure 5b. In particular, the latter visualizes the high non-linearity and inelasticity of skin tissue.

The magnitude of deformation is determined by a number of factors such as moisture content of skin, region of measurement, pressure applied to the skin upon probe placement, and most significantly, inter-subject variability. Nonetheless, as the presented data together with previous Cutometer and other suction experiments [9, 41] have shown so far, sufficient repeatability is provided, which is a fundamental prerequisite when using these data for model parameter identification including multiple measurement curves.

7.2. The finite element model of the inverse problem

The FE model used for this study is based on the work presented by Barbarino *et al.* [41]. The model consists of two tissue layers, representing the most superficial layer skin and the SMAS underneath. The interaction between both layers is modeled such that no relative displacement or slipping may occur. The respective thicknesses of 1.7 mm for skin and 3.0 mm for SMAS were determined from ultrasound measurements in the face of the 29-year-old male subject of this study. Material parameters for SMAS are taken from Mazza *et al.* [16], while a new set of skin parameters is determined as presented in Section 7.3.

The FE mesh was optimized for sufficient refinement in regions of larger strains and the contact zone between skin and probe (Figure 6). Furthermore, the choice of boundary conditions on the model, initial shear modulus (stiffness) and thickness of SMAS, and contact definition between probe and skin were tested in order to validate the FE model assumptions. An elaborate analysis of the model's sensitivity to changes in these properties is presented in Section 7.4.

Because of the nature of the Cutometer measurement with respect to the size of the probe's small aperture diameter and its circular shape, the material's apparent anisotropy [77] is assumed to have a marginal impact on the resulting apex height. Therefore and without loss of generality, skin is considered to be an isotropic material in the FE model presented here. Indeed, the evaluation of suction-based experimental characterization of skin is often interpreted on the basis of assuming an isotropic material response [67, 78–80]. To the contrary, suction experiments with a large and elliptically shaped probe aperture presented by Iivarinen *et al.* [68] were used in order to

DOI: 10.1002/cnm

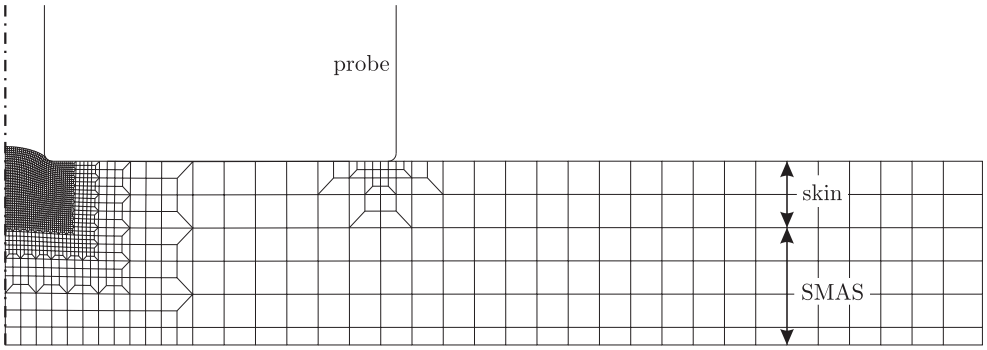

Figure 6. Finite element model for the inverse problem of the Cutometer experiment shown in the deformed state. The bottom nodes are fixed against vertical displacement, while no boundary conditions are imposed on nodes on the right side of the model. SMAS, superficial muscular aponeurotic system.

potentially capture the anisotropic tissue response and to include this information in the determination of anisotropic material properties.

7.3. Parameter identification for facial skin

The identification of representative model parameters is an essential component in realistic simulation of tissue response in surgery planning, implant design, wrinkle formation during facial expressions, and aging. Based on the experimental campaign and the FE model presented in Sections 7.1 and 7.2, an inverse problem is set up to determine a set of parameters, which provides a good agreement between experimental data and the numerical simulation.

Out of the six different averaged measurement curves, three were chosen for the optimization of parameters and the remaining other three used for verification of the set. The averaged measurement curves of instant loading at 300 and 500 mbar, as well as the tissue response upon linear loading and unloading at a pressure rate of 15 mbar/s, were used as input for the objective functions in the inverse problem. Using the *fminsearch procedure* in Matlab (Matlab 10.0, The MathWorks, Inc., Natick, MA, USA) with the Nelder–Mead simplex algorithm, the difference between the measurement curves and the corresponding numerical simulations was minimized. The parameters that were included in the optimization were chosen based on their relevance with respect to the two different types of measurements. The shape of initial loading is mainly determined by μ_0, q, m_2, and Γ_2. Γ_1 and r_2 are included in order to allow for adopting the material parameters to fit the linear loading and unloading experiments at different strain rates. Furthermore, the parameter m_5 was chosen to be $1 - m_2$. The remaining material parameters are based on the work by Mazza *et al.* [16] and are chosen to exhibit a specific model response (Table III). In particular, m_1 was set to a sufficiently large number in order to enforce the incompressibility of the tissue, and m_3 was set to zero because of the isotropy assumption of the skin.

The optimization routine provided a set of material parameters that well represents the experimental data as summarized in Figure 7. In particular, not only is the maximum apex height of the tissue bubble well predicted in all six cases but the experimentally observed tissue recovery in the case of linear unloading is also well represented. For the measurement with linearly increasing and decreasing pressures at a constant pressure rate, the Cutometer reveals limitations in pressure control for pressures below 25 mbar. During the initial phase of loading and the final phase of unloading, the pressure rate is insufficiently controlled, leading to exaggerated loading and unloading of the tissue by the Cutometer, respectively. The data presented in Figure 6 clearly shows this effect through a

Table III. Model parameters from the literature [16].

m_1	m_3	m_4	n	r_1	r_3	r_4	r_5
1000.0	0.0	1.0	0.5	20.0	10^{-10}	10^{-4}	1.0

DOI: 10.1002/cnm

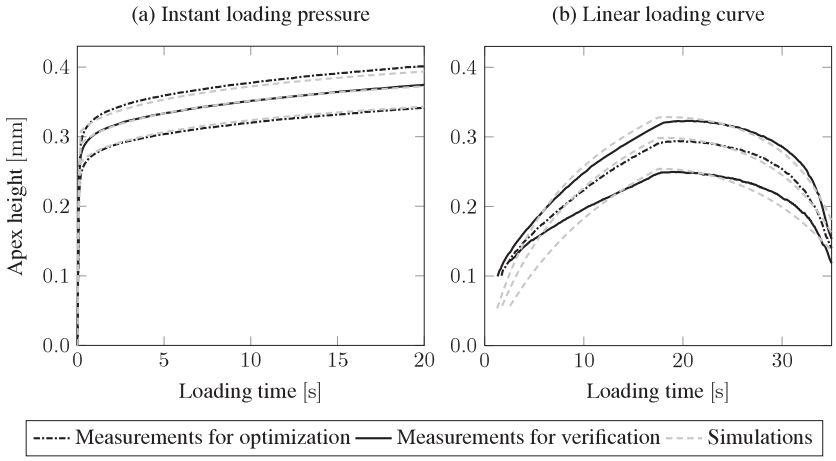

Figure 7. Results of the least square optimization. Comparison between Cutometer measurements and numerical simulation for the (a) instant loading and (b) the linearly loading and unloading cases.

Table IV. Model parameters from parameter identification for human facial skin.

μ_0 (kPa)	q	m_2	Γ_1	Γ_2	r_2
0.18	43.0	$3.87 \cdot 10^{-5}$	1.46	67.45	8.25

pronounced slope at the beginning and end of each measurement. For this reason, experimental and numerical data in Figure 7b are shown for pressures greater than 25 mbar only. This deficiency of the Cutometer explains the observed discrepancy between experimental and numerical data in the initial loading and final unloading phases.

The parameters identified with the presented routine are given in Table IV. The numerical value of the initial shear modulus $\mu_0 = 0.18\,\text{kPa}$ is well within values presented in the literature [41, 67, 81, 82]. Moreover, the small value of $m_2 = 3.87 \cdot 10^{-5}$ can be explained by the predominant response of the skin as a dissipative elastic tissue as well as the rather short-term tissue response considered in the two Cutometer measurement protocols. A longer hold period in the case of instant loading pressure and/or a longer ramping pressure would provide more information regarding the long-term response of the tissue and influence m_2, which mainly controls the purely elastic distortional response.

7.4. Sensitivity analysis of the finite element model

The FE model presented by Barbarino *et al.* [41] and used in the present study has been thoroughly investigated with respect to the assumptions on boundary conditions, material properties of SMAS, thickness of SMAS, and the interaction between probe and skin tissue. The impact of these assumptions at the basis of this FE model was verified using the newly determined material parameters, and the results are presented in terms of the relative error defined by

$$\text{error}_{\text{rel}} = \frac{\max\left[u^{\text{ref}}\right] - \max\left[u^{C_i}\right]}{\max\left[u^{\text{ref}}\right]} \cdot 100, \tag{49}$$

where $\max[u^{\text{ref}}]$ is the maximum apex height obtained by the reference model and $\max[u^{C_i}]$ is the maximum apex height obtained by the different simulations C_i, where $i = 1, \ldots, 9$ (Figure 8). Both Cutometer measurement protocols considered in this study are verified here, in order to demonstrate the FE model's wide range of applicability.

It can be seen from Figure 8 that the variation of fundamental FE model parameters has only a marginal impact of at most 5.12% on the overall apex response when considering a variation of the

DOI: 10.1002/cnm

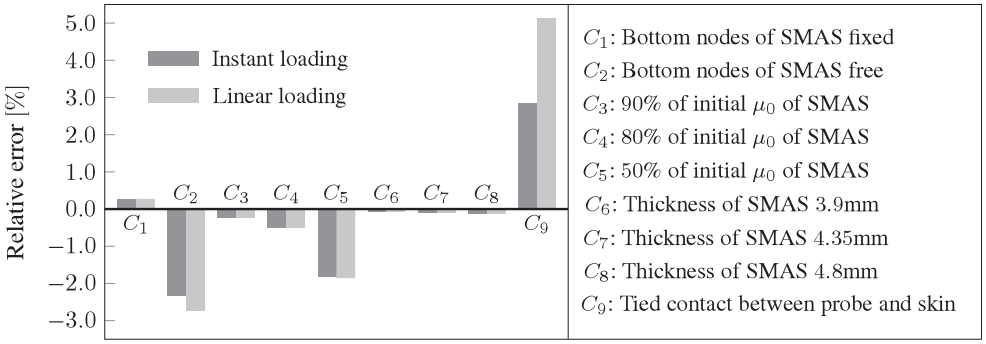

Figure 8. Sensitivity analysis on the finite element model used for the parameter identification. Results shown as relative errors of apex height for the reference simulation and the corresponding simulation with a varied parameter. SMAS, superficial muscular aponeurotic system.

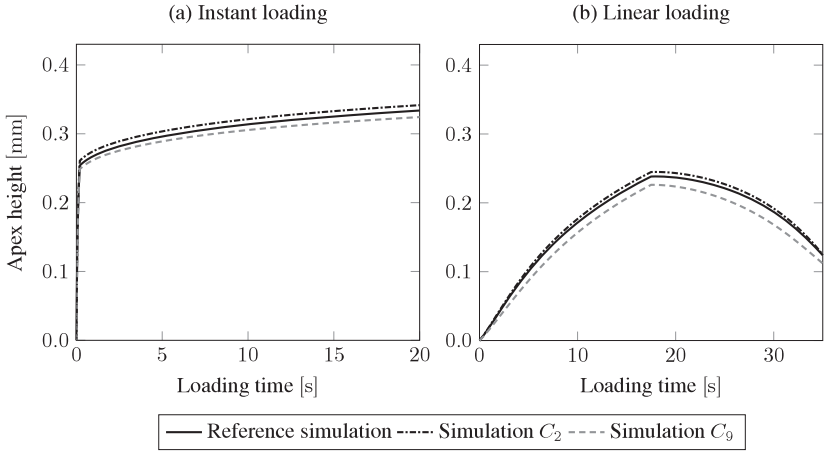

Figure 9. Sensitivity analysis on the finite element model used for the parameter identification. Apex displacement for the reference simulation and simulations C_1, C_2, and C_9 upon (a) instant loading and (b) linear loading and unloading.

parameters in a physical range. The most crucial impact on the overall tissue behavior arises from the choice of the interaction properties between probe and skin. The relative error between both extreme cases of frictionless and rough contact is 5.12% for the linearly varying loading profile and less than 2.85% in the case of instant loading. This rather marginal variation is also reflected in an only slightly influenced shape of the apex displacement curve as shown in Figure 9 (simulation C_9). As to be expected, a tied contact between probe and skin leads to a reduced apex height as the inward suction of tissue is restricted.

The presented results also disclose the effect of the boundary conditions on the bottom nodes of SMAS. The two extreme cases of fixing horizontal and vertical displacements (C_1) and removing any constraint on these nodes (C_2) lead to a minor difference in the total apex deformation ($+0.26\%$ and -2.33% for instant loading and $+0.27\%$ and -2.74% for linear loading).

The intervariability of the stiffness of SMAS was studied by reducing the initial shear modulus μ_0 by 10%, 20%, and 50% (C_3, C_4, and C_5). It was found that such a variation has a marginal impact on the skin tissue response. In particular, a reduction by 50% resulted in an increased maximum apex height of 1.82% and 1.86% for the two different measurement protocols. It should be noted that in our study, the material properties of SMAS were adopted from Mazza *et al.* [16]. However, there is a need to conduct further experimental measurements to properly define the material properties of SMAS. This should include suction method-based experiments with a larger probe aperture diameter in order to ensure the penetration of deeper tissue layers as presented by [9, 23, 41]. The impact

DOI: 10.1002/cnm

of the thickness of SMAS on the overall response of skin is found to be less than 0.12% for an increased tissue thickness of up to 33%.

Figure 9 shows the apex displacement history of both measurement protocols for a selection of simulations within the sensitivity analysis. The two extreme cases C_2 (bottom nodes of SMAS free) and C_9 (tied contact between probe and skin) represent the upper and lower bounds of the tissue mechanical response in the study presented here. The remaining simulations predict a tissue response within these two curves.

In conclusion, the FE model is broadly based on physically valid assumptions with respect to the thickness of both tissues, the choice of boundary conditions on the individual layers, and a realistic representation of the interaction between probe and skin. Moreover, the presented results strongly demonstrate that a variation in relevant model parameters has a marginal impact on the predicted tissue response independent of the type of loading profile considered in the numerical simulation.

8. CONCLUSION

In the face of the significant challenges with respect to the numerical implementation of elastic–viscoplastic constitutive equations describing the highly nonlinear and time-dependent mechanical response of soft tissues, a new mixed FE formulation based on the relative deformation gradient is developed for a generalized framework of constitutive equations of elastic–viscoplastic soft biological tissues. In the present paper, the constitutive equations proposed by Rubin and Bodner [46] were considered as a particular case and are used for the numerical study. The introduction of the relative deformation gradient leads to a formulation that is based on the last converged and current configurations, instead of the dependence on the reference and current deformed configurations. Such dependence is particularly suitable for constitutive equations that are formulated in terms of rate of deformation measures. The developed FE formulation was implemented in the commercial FE package Abaqus [62], and the implementation was validated through standard numerical tests including patch test, rate of convergence, and objectivity test. It was found that the formulation passed the patch test, exhibited quadratic convergence, and showed the integration scheme to be unaffected by superposed rigid body rotation.

Furthermore, an experimental campaign was conducted, which aims at characterizing the mechanical tissue response of facial skin by means of the multiaxial loading state resulting from suction tests. Specifically, two different loading protocols were defined in order to provide sufficient data for the determination of a set of material model parameters. This set was identified by iteratively solving the inverse FE problem. A comparison between the experimental data and the numerical simulations demonstrated the model's capabilities to represent the highly nonlinear tissue behavior of the skin. This represents a valuable improvement of the model's applicability over previously presented material model parameters. Rubin and Bodner [46] and Mazza *et al.* [16] provide two different sets of parameters based on the same experimental data on uniaxially tested excised skin tissue strips, which have both been shown to significantly overestimate the tissue's stiffness in physically relevant multiaxial loading conditions.

The present study is conducted in the framework of realistic simulation of facial tissue during facial expressions, mastication, and aging [41, 55, 83, 84]. To this end, the model implementation within a numerically robust FE formulation is a significant step in the attempt to represent the physical tissue response in complex tissue structures. Further steps should include the characterization of deeper tissue layers by means of the suction method using a larger diameter for the probe opening in order to determine material model parameters for a more physical loading state in comparison with uniaxial stress tests. Moreover, the experimental campaign should be extended to investigate anisotropy of facial skin tissue, as well as the mechanical response to cyclic loading. Consequently, the inverse FE problem model needs to be adopted to allow for the determination of corresponding material parameters.

The numerical performance of the new framework for the implementation of elastic–viscoplastic material models should be further analyzed with respect to convergence behavior, especially for cases of high-rate and large deformation as in traumatic brain injury or traumatic aortic rupture.

DOI: 10.1002/cnm

APPENDIX A

Table A1. Material parameters of the Rubin and Bodner model [46].

μ_0, μ	Initial and nonlinear shear modulus
q	Parameter influencing the nonlinearity of the strain energy function W
$m_1 - m_5$	Parameters of the additive function g in the strain energy function W
$r_1 - r_5$	Parameters of the evolution equation of the hardening function β
Γ_1, Γ_2, n	Parameters of the rate of inelasticity function Γ

Table A2. Nomenclature.

$\mathbf{X}, \mathbf{x}$	Location of a material point in the reference and current configurations
$\mathbf{F}, \mathbf{l}, \mathbf{d}$	Deformation gradient, velocity gradient, and rate of deformation tensor
$\mathbf{b}, \mathbf{b}'$	Total deformation tensor and total elastic distortional deformation tensor
$\mathbf{b}'_{de}$	Elastic distortional deformation associated with the dissipative component
J	Total dilatation
$\mathbf{a}_d$	Direction of the inelastic flow
Γ	Magnitude of the rate of inelasticity
$\dot{\varepsilon}$	Effective total distortional deformation rate
β	Hardening measure
β_{de}	Effective elastic distortion strain associated with the dissipative component
β_1, β_2	First and second invariants of the total deformation tensor
α_1, α_2	First and second invariants of $\mathbf{b}'_{de}$
$\mathbf{M}_I, \mathbf{m}_I$	Orientation of the I'th fiber family in the reference and current configurations
λ_I	Stretch of the I'th fiber family
W	Strain energy function
$\boldsymbol{\sigma}, \boldsymbol{\tau}$	Cauchy and Kirchhoff stress tensor
$\mathbf{F}_r$	Relative deformation gradient
J_r	Relative total dilatation
$\mathbf{C}_r, \mathbf{b}_r$	Relative right Cauchy–Green deformation tensor and relative deformation tensor
$\bar{\mathbf{F}}$	Modified deformation gradient
$\mathbf{b}'^{*}_{de}$	Elastic trial of $\mathbf{b}'_{de}$
a	Spatial tangent moduli
$\bar{J}_r$	Assumed relative averaged volumetric dilatation
$\bar{p}$	Assumed averaged hydrostatic pressure
$\delta\mathbf{u}, \Delta\mathbf{u}$	Virtual and incremental displacement vectors
$\delta\mathbf{h}, \Delta\mathbf{h}$	Virtual and incremental displacement gradients
$\delta\underline{\mathbf{d}}_u, \Delta\underline{\mathbf{d}}_u$	Virtual and incremental nodal displacement vectors
$\widehat{\underline{\mathbf{r}}}$	Residual forces
$\underline{\underline{\mathbb{B}}}$	Standard **B**-matrix in finite elements
$\underline{\underline{K}}$	Tangent stiffness matrix

APPENDIX B

The spatial tangent moduli for the generalized viscoplastic model are defined by

$$\mathsf{a} = \left[\frac{\partial W}{\partial J} + J\frac{\partial^2 W}{\partial J \partial J}\right]\mathbf{I}\otimes\mathbf{I} + \frac{4}{J}\frac{\partial^2 W}{\partial \beta_1 \partial \beta_1}\mathrm{dev}\left(\mathbf{b}'\right)\otimes\mathrm{dev}\left(\mathbf{b}'\right) + \frac{16}{J}\frac{\partial^2 W}{\partial \beta_2 \partial \beta_2}\mathrm{dev}\left(\mathbf{b}'^2\right)\otimes\mathrm{dev}\left(\mathbf{b}'^2\right) + \frac{2}{J}\frac{\partial^2 W}{\partial \alpha_1 \partial \alpha_1}\mathrm{dev}\left(\mathbf{b}'_{de}\right)\otimes\boldsymbol{\alpha}_1$$

DOI: 10.1002/cnm

$$
\begin{aligned}
&+\frac{4}{J}\frac{\partial^2 W}{\partial\alpha_2\partial\alpha_2}\mathrm{dev}\left(\mathbf{b}_{de}'^2\right)\otimes\boldsymbol{\alpha}_2+\sum_{I=1}^{N_{\text{fib.}}}\sum_{J=1}^{N_{\text{fib.}}}\frac{1}{J\lambda_I\lambda_J}\frac{\partial^2 W}{\partial\lambda_I\partial\lambda_J}\left(\mathbf{m}_I\otimes\mathbf{m}_I\right)\otimes\left(\mathbf{m}_J\otimes\mathbf{m}_J\right)\\
&+\sum_{I=1}^{N_{\text{fib.}}}\frac{1}{J\lambda_I^3}\frac{\partial^2 W}{\partial\lambda_I\partial\lambda_I}\left(\mathbf{m}_I\otimes\mathbf{m}_I\right)\otimes\left(\mathbf{m}_I\otimes\mathbf{m}_I\right)+2\frac{\partial^2 W}{\partial J\,\partial\beta_1}\left[\mathrm{dev}\left(\mathbf{b}'\right)\otimes\mathbf{I}+\mathbf{I}\otimes\mathrm{dev}\left(\mathbf{b}'\right)\right]\\
&+4\frac{\partial^2 W}{\partial J\,\partial\beta_2}\left[\mathrm{dev}\left(\mathbf{b}'^2\right)\otimes\mathbf{I}+\mathbf{I}\otimes\mathrm{dev}\left(\mathbf{b}'^2\right)\right]+\frac{\partial^2 W}{\partial J\,\partial\alpha_1}\left[2\mathrm{dev}\left(\mathbf{b}_{de}'\right)\otimes\mathbf{I}+\mathbf{I}\otimes\boldsymbol{\alpha}_1\right]\\
&+\frac{\partial^2 W}{\partial J\,\partial\alpha_2}\left[4\mathrm{dev}\left(\mathbf{b}_{de}'^2\right)\otimes\mathbf{I}+\mathbf{I}\otimes\boldsymbol{\alpha}_2\right]+\sum_{I=1}^{N_{\text{fib.}}}\frac{1}{\lambda_I}\frac{\partial^2 W}{\partial J\,\partial\lambda_I}\left[\left(\mathbf{m}_I\otimes\mathbf{m}_I\right)\otimes\mathbf{I}+\mathbf{I}\otimes\left(\mathbf{m}_I\otimes\mathbf{m}_I\right)\right]\\
&+\frac{8}{J}\frac{\partial^2 W}{\partial\beta_1\partial\beta_2}\left[\mathrm{dev}\left(\mathbf{b}'^2\right)\otimes\mathrm{dev}\left(\mathbf{b}'\right)+\mathrm{dev}\left(\mathbf{b}'\right)\otimes\mathrm{dev}\left(\mathbf{b}'^2\right)\right]\\
&+\frac{2}{J}\frac{\partial^2 W}{\partial\beta_1\partial\alpha_1}\left[2\mathrm{dev}\left(\mathbf{b}_{de}'\right)\otimes\mathrm{dev}\left(\mathbf{b}'\right)+\mathrm{dev}\left(\mathbf{b}'\right)\otimes\boldsymbol{\alpha}_1\right]\\
&+\frac{2}{J}\frac{\partial^2 W}{\partial\beta_1\partial\alpha_2}\left[2\mathrm{dev}\left(\mathbf{b}_{de}'^2\right)\otimes\mathrm{dev}\left(\mathbf{b}'\right)+\mathrm{dev}\left(\mathbf{b}'\right)\otimes\boldsymbol{\alpha}_2\right]\\
&+\sum_{I=1}^{N_{\text{fib.}}}\frac{2}{J\lambda_I}\frac{\partial^2 W}{\partial\beta_1\partial\lambda_I}\left[\left(\mathbf{m}_I\otimes\mathbf{m}_I\right)\otimes\mathrm{dev}\left(\mathbf{b}'\right)+\mathrm{dev}\left(\mathbf{b}'\right)\otimes\left(\mathbf{m}_I\otimes\mathbf{m}_I\right)\right]\\
&+\frac{4}{J}\frac{\partial^2 W}{\partial\beta_2\partial\alpha_1}\left[2\mathrm{dev}\left(\mathbf{b}_{de}'\right)\otimes\mathrm{dev}\left(\mathbf{b}'^2\right)+\mathrm{dev}\left(\mathbf{b}'^2\right)\otimes\boldsymbol{\alpha}_1\right]\\
&+\frac{4}{J}\frac{\partial^2 W}{\partial\beta_2\partial\alpha_2}\left[4\mathrm{dev}\left(\mathbf{b}_{de}'^2\right)\otimes\mathrm{dev}\left(\mathbf{b}'^2\right)+\mathrm{dev}\left(\mathbf{b}'^2\right)\otimes\boldsymbol{\alpha}_2\right]\\
&+\sum_{I=1}^{N_{\text{fib.}}}\frac{4}{J\lambda_I}\frac{\partial^2 W}{\partial\beta_2\partial\lambda_I}\left[\left(\mathbf{m}_I\otimes\mathbf{m}_I\right)\otimes\mathrm{dev}\left(\mathbf{b}'^2\right)+\mathrm{dev}\left(\mathbf{b}'^2\right)\otimes\left(\mathbf{m}_I\otimes\mathbf{m}_I\right)\right]\\
&+\frac{1}{J}\frac{\partial^2 W}{\partial\alpha_1\partial\alpha_2}\left[4\mathrm{dev}\left(\mathbf{b}_{de}'^2\right)\otimes\boldsymbol{\alpha}_1+2\mathrm{dev}\left(\mathbf{b}_{de}'\right)\otimes\boldsymbol{\alpha}_2\right]\\
&+\sum_{I=1}^{N_{\text{fib.}}}\frac{1}{J\lambda_I}\frac{\partial^2 W}{\partial\alpha_1\partial\lambda_I}\left[\left(\mathbf{m}_I\otimes\mathbf{m}_I\right)\otimes\boldsymbol{\alpha}_1+2\mathrm{dev}\left(\mathbf{b}_{de}'\right)\otimes\left(\mathbf{m}_I\otimes\mathbf{m}_I\right)\right]\\
&+\sum_{I=1}^{N_{\text{fib.}}}\frac{1}{J\lambda_I}\frac{\partial^2 W}{\partial\alpha_2\partial\lambda_I}\left[\left(\mathbf{m}_I\otimes\mathbf{m}_I\right)\otimes\boldsymbol{\alpha}_2+4\mathrm{dev}\left(\mathbf{b}_{de}'^2\right)\otimes\left(\mathbf{m}_I\otimes\mathbf{m}_I\right)\right]\\
&+\frac{2}{J}\frac{\partial W}{\partial\beta_1}\frac{\partial\mathrm{dev}\left(\mathbf{b}'\right)}{\partial\mathbf{F}_r}\mathbf{F}_r^{\mathsf{T}}+\frac{4}{J}\frac{\partial W}{\partial\beta_2}\frac{\partial\mathrm{dev}\left(\mathbf{b}'^2\right)}{\partial\mathbf{F}_r}\mathbf{F}_r^{\mathsf{T}}+\frac{2}{J}\frac{\partial W}{\partial\alpha_1}\frac{\partial\mathrm{dev}\left(\mathbf{b}_{de}'\right)}{\partial\mathbf{F}_r}\mathbf{F}_r^{\mathsf{T}}\\
&+\frac{4}{J}\frac{\partial W}{\partial\alpha_2}\frac{\partial\mathrm{dev}\left(\mathbf{b}_{de}'^2\right)}{\partial\mathbf{F}_r}\mathbf{F}_r^{\mathsf{T}}+\sum_{I=1}^{N_{\text{fib.}}}\frac{1}{J\lambda_I}\frac{\partial W}{\partial\lambda_I}\frac{\partial\left(\mathbf{m}_I\otimes\mathbf{m}_I\right)}{\partial\mathbf{F}_r}\mathbf{F}_r^{\mathsf{T}}
\end{aligned}
\tag{B.1}
$$

APPENDIX C

The coefficients $\{d_0\left(t_{n+1}\right),\ d_1\left(t_{n+1}\right),\ d_2\left(t_{n+1}\right)\}$ that are used in (28) are given by

$$
d_0\left(t_{n+1}\right)=1-\Delta t\frac{\dfrac{\partial\widehat{\Gamma}}{\partial\beta}\left(\dfrac{\partial\widehat{\beta}}{\partial\Gamma}+\dfrac{\partial\widehat{\beta}}{\partial\beta_{de}}\dfrac{\partial\beta_{de}}{\partial\Gamma}\right)}{1-\Delta t\dfrac{\partial\widehat{\beta}}{\partial\beta}}-\frac{\partial\widehat{\Gamma}}{\partial\beta_{de}}\frac{\partial\beta_{de}}{\partial\Gamma},
$$

DOI: 10.1002/cnm

$$d_1(t_{n+1}) = \frac{\partial \widehat{\Gamma}}{\partial \dot{\varepsilon}} + \Delta t \frac{\dfrac{\partial \widehat{\Gamma}}{\partial \beta}\dfrac{\partial \widehat{\beta}}{\partial \dot{\varepsilon}}}{1 - \Delta t \dfrac{\partial \widehat{\beta}}{\partial \beta}},$$
$$d_2(t_{n+1}) = \left(\frac{\partial \widehat{\Gamma}}{\partial \beta_{de}} + \Delta t \frac{\dfrac{\partial \widehat{\Gamma}}{\partial \beta}\dfrac{\partial \widehat{\beta}}{\partial \beta_{de}}}{1 - \Delta t \dfrac{\partial \widehat{\beta}}{\partial \beta}} \right) \frac{\partial \beta_{de}}{\partial \beta^*_{de}}. \tag{C.1}$$

REFERENCES

1. Fung Y. *Biomechanics: Mechanical Properties of Living Tissues*. Springer: New York, 1993.
2. Bischoff J, Arruda E, Grosh K. A rheological network model for the continuum anisotropic and viscoelastic behavior of soft tissue. *Biomechanics and Modeling in Mechanobiology* 2004; **3**(1):56–65.
3. Buerzle W, Haller C, Jabareen M, Egger J, Mallik A, Ochsenbein-Koelble N, Ehrbar M, Mazza E. Multiaxial mechanical behavior of human fetal membranes and its relationship to microstructure. *Biomechanics and Modeling in Mechanobiology* 2013; **12**(4):747–762.
4. Ehret A, Itskov M. Modeling of anisotropic softening phenomena: application to soft biological tissues. *International Journal of Plasticity* 2009; **25**(5):901–919.
5. Barbarino GG, Jabareen M, Mazza E. Experimental and numerical study of the relaxation behavior of facial soft tissue. *PAMM* 2009; **9**(1):87–90.
6. Göktepe S, Abilez O, Parker K, Kuhl E. A multiscale model for eccentric and concentric cardiac growth through sarcomerogenesis. *Journal of Theoretical Biology* 2010; **265**(3):433–442.
7. Menzel A, Kuhl E. Frontiers in growth and remodeling. *Mechanics Research Communications* 2012; **42**:1–14.
8. Zöllner A, Abilez O, Böl M, Kuhl E. Stretching skeletal muscle: chronic muscle lengthening through sarcomerogenesis. *PLoS ONE* 2012; **7**(10):Article ID: e45661, 10p.
9. Badir S, Mazza E, Zimmermann R, Bajka M. Cervical softening occurs early in pregnancy: characterization of cervical stiffness in 100 healthy women using the aspiration technique. *Prenatal Diagnosis* 2013; **33**(8):737–741.
10. Maher E, Creane A, Lally C, Kelly D. An anisotropic inelastic constitutive model to describe stress softening and permanent deformation in arterial tissue. *Journal of the Mechanical Behavior of Biomedical Materials* 2012; **12**:9–19.
11. Alastrué V, Rodríguez J, Calvo B, Doblaré M. Structural damage models for fibrous biological soft tissues. *International Journal of Solids and Structures* 2007; **44**(18–19):5894–5911.
12. Marini G, Maier A, Reeps C, Eckstein HH, Wall W, Gee M. A continuum description of the damage process in the arterial wall of abdominal aortic aneurysms. *International Journal for Numerical Methods in Biomedical Engineering* 2012; **28**(1):87–99.
13. Martin C, Sun W. Modeling of long-term fatigue damage of soft tissue with stress softening and permanent set effects. *Biomechanics and Modeling in Mechanobiology* 2013; **12**(4):645–655.
14. Sáez P, Alastrué V, Peña E, Doblaré M, Martínez M. Anisotropic microsphere-based approach to damage in soft fibered tissue. *Biomechanics and Modeling in Mechanobiology* 2012; **11**(5):595–608.
15. Epstein M. The split between remodelling and aging. *International Journal of Non-Linear Mechanics* 2009; **44**(6):604–609.
16. Mazza E, Papes O, Rubin M, Bodner S, Binur N. Nonlinear elastic–viscoplastic constitutive equations for aging facial tissues. *Biomechanics and Modeling in Mechanobiology* 2005; **4**(2-3):178–189.
17. Kuhl E, Holzapfel G. A continuum model for remodeling in living structures. *Journal of Materials Science* 2007; **42**(21):8811–8823.
18. Sáez P, Peña E, Angel Martínez M, Kuhl E. Mathematical modeling of collagen turnover in biological tissue. *Journal of Mathematical Biology* 2013; **67**(6–7):1765–1793.
19. Sverdlik A, Lanir Y. Time-dependent mechanical behavior of sheep digital tendons, including the effects of preconditioning. *Journal of Biomechanical Engineering* 2002; **124**(1):78–84.
20. Provenzano P, Lakes R, Keenan T, Vanderby R, Jr. Nonlinear ligament viscoelasticity. *Annals of Biomedical Engineering* 2001; **29**(10):908–914.
21. Nekouzadeh A, Pryse KM, Elson EL, Genin GM. A simplified approach to quasi-linear viscoelastic modeling. *Journal of Biomechanics* 2007; **40**(14):3070–3078.
22. Bischoff J. Reduced parameter formulation for incorporating fiber level viscoelasticity into tissue level biomechanical models. *Annals of Biomedical Engineering* 2006; **34**(7):1164–1172.
23. Nava A, Mazza E, Kleinermann F, Avis N, McClure J, Bajka M. Evaluation of the mechanical properties of human liver and kidney through aspiration experiments. *Technology and Health Care* 2004; **12**(3):269–280.
24. Vena P, Gastaldi D, Contro R. A constituent-based model for the nonlinear viscoelastic behavior of ligaments. *Journal of Biomechanical Engineering* 2006; **128**(3):449–457.

DOI: 10.1002/cnm

25. Nguyen T, Jones R, Boyce B. Modeling the anisotropic finite-deformation viscoelastic behavior of soft fiber-reinforced composites. *International Journal of Solids and Structures* 2007; **44**(25–26):8366–8389.
26. Le Tallec P, Rahier C, Kaiss A. Three-dimensional incompressible viscoelasticity in large strains: formulation and numerical approximation. *Computer Methods in Applied Mechanics and Engineering* 1993; **109**(3–4):233–258.
27. Holzapfel G, Simo J. A new viscoelastic constitutive model for continuous media at finite thermomechanical changes. *International Journal of Solids and Structures* 1996; **33**(20–22):3019–3034.
28. Govindjee S, Reese S. A presentation and comparison of two large deformation viscoelasticity models. *Journal of Engineering Materials and Technology, Transactions of the ASME* 1997; **119**(3):251–255.
29. Holzapfel G, Gasser T. A viscoelastic model for fiber-reinforced composites at finite stains: continuum basis, computational aspects and applications. *Computer Methods in Applied Mechanics and Engineering* 2001; **190**(34): 4379–4403.
30. Holzapfel G, Gasser T, Stadler M. A structural model for the viscoelastic behavior of arterial walls: continuum formulation and finite element analysis. *European Journal of Mechanics, A/Solids* 2002; **21**(3):441–463.
31. Peña E, Calvo B, Martínez M, Doblaré M. An anisotropic visco-hyperelastic model for ligaments at finite strains. Formulation and computational aspects. *International Journal of Solids and Structures* 2007; **44**(3–4):760–778.
32. Peña E, Calvo B, Martínez M, Doblaré M. On finite-strain damage of viscoelastic-fibred materials. Application to soft biological tissues. *International Journal for Numerical Methods in Engineering* 2008; **74**(7):1198–1218.
33. Ehret A. Generalised concepts for constitutive modelling of soft biological tissues. *Dissertation*, 2011.
34. Famaey N, Vander Sloten J, Kuhl E. A three-constituent damage model for arterial clamping in computer-assisted surgery. *Biomechanics and Modeling in Mechanobiology* 2013; **12**(1):123–136.
35. Peña E, Alastrué V, Laborda A, Martínez M, Doblaré M. A constitutive formulation of vascular tissue mechanics including viscoelasticity and softening behaviour. *Journal of Biomechanics* 2010; **43**(5):984–989.
36. Balzani D, Brinkhues S, Holzapfel G. Constitutive framework for the modeling of damage in collagenous soft tissues with application to arterial walls. *Computer Methods in Applied Mechanics and Engineering* 2012; **213–216**: 139–151.
37. Schröder J, Balzani D, Gross D. Aspects of modeling and computer simulation of soft tissues: applications to arterial walls. *Materialwissenschaft und Werkstofftechnik* 2005; **36**(12):795–801.
38. Mullins L. Effect of stretching on the properties of rubber. *Rubber Chemistry and Technology* 1948; **21**(2):281–300.
39. Hollenstein M, Ehret A, Itskov M, Mazza E. A novel experimental procedure based on pure shear testing of dermatome-cut samples applied to porcine skin. *Biomechanics and Modeling in Mechanobiology* 2011; **10**(5): 651–661.
40. Boyce B, Jones R, Nguyen T, Grazier J. Stress-controlled viscoelastic tensile response of bovine cornea. *Journal of Biomechanics* 2007; **40**(11):2367–2376.
41. Barbarino G, Jabareen M, Mazza E. Experimental and numerical study on the mechanical behavior of the superficial layers of the face. *Skin Research and Technology* 2011; **17**(4):434–444.
42. Pini M, Zysset P, Botsis J, Contro R. Tensile and compressive behaviour of the bovine periodontal ligament. *Journal of Biomechanics* 2004; **37**(1):111–119.
43. Buerzle W, Mazza E. On the deformation behavior of human amnion. *Journal of Biomechanics* 2013; **46**(11): 1777–1783.
44. Franceschini G, Bigoni D, Regitnig P, Holzapfel G. Brain tissue deforms similarly to filled elastomers and follows consolidation theory. *Journal of the Mechanics and Physics of Solids* 2006; **54**(12):2592–2620.
45. García A, Martínez M, Peña E. Determination and modeling of the inelasticity over the length of the porcine carotid artery. *Journal of Biomechanical Engineering* 2013; **135**(3):9p.
46. Rubin M, Bodner S. A three-dimensional nonlinear model for dissipative response of soft tissue. *International Journal of Solids and Structures* 2002; **39**(19):5081–5099.
47. Balzani D, Schröder J, Gross D. Simulation of discontinuous damage incorporating residual stresses in circumferentially overstretched atherosclerotic arteries. *Acta Biomaterialia* 2006; **2**(6):609–618.
48. Gasser TC. An irreversible constitutive model for fibrous soft biological tissue: a 3- D microfiber approach with demonstrative application to abdominal aortic aneurysms. *Acta Biomaterialia* 2011; **7**(6):2457–2466.
49. Peña J, Martínez M, Peña E. A formulation to model the nonlinear viscoelastic properties of the vascular tissue. *Acta Mechanica* 2011; **217**(1–2):63–74.
50. Perzyna P. Thermodynamic theory of viscoplasticity. *Advances in Applied Mechanics* 1971; **11**(C):313–354.
51. Eckart C. The thermodynamics of irreversible processes. IV. The theory of elasticity and anelasticity. *Physical Review* 1948; **73**(4):373–382.
52. Rubin M, Attia A. Calculation of hyperelastic response of finitely deformed elastic–viscoplastic materials. *International Journal for Numerical Methods in Engineering* 1996; **39**(2):309–320.
53. Rubin M. Removal of unphysical arbitrariness in constitutive equations for elastically anisotropic nonlinear elastic-viscoplastic solids. *International Journal of Engineering Science* 2012; **53**:38–45.
54. Volokh K. An approach to elastoplasticity at large deformations. *European Journal of Mechanics, A/Solids* 2013; **39**:153–162.
55. Barbarino G, Jabareen M, Trzewik J, Nkengne A, Stamatas G, Mazza E. Development and validation of a three-dimensional finite element model of the face. *Journal of Biomechanical Engineering* 2009; **131**(4):11 p.
56. Besseling JF. A thermodynamic approach to rheology. In *Irreversible Aspects of Continuum Mechanics and Transfer of Physical Characteristics in Moving Fluids*, Parkus H, Sedov LI (eds)., IUTAM Symposia. Springer: Vienna, 1968; 16–53.

DOI: 10.1002/cnm

57. Leonov A. Nonequilibrium thermodynamics and rheology of viscoelastic polymer media. *Rheologica Acta* 1976; **15**(2):85–98.
58. Papes O. Nonlinear continuum mechanics in modern engineering applications. *Dissertation ETH Zürich: Nr.19956*, 2011.
59. Rubin M, Papes O. Advantages of formulating evolution equations for elastic–viscoplastic materials in terms of the velocity gradient instead of the spin tensor. *Journal of Mechanics of Materials and Structures* 2011; **6**(1–4):529–543.
60. Simo J. Algorithms for static and dynamic multiplicative plasticity that preserve the classical return mapping schemes of the infinitesimal theory. *Computer Methods in Applied Mechanics and Engineering* 1992; **99**(1):61–112.
61. Simo J, Hughes T. *Computational Inelasticity*. Springer-Verlag: New York, 1998.
62. ABAQUS. *ABAQUS/Standard Analysis Users Manual.* Dassault Systems: Providence, RI, USA, 2009.
63. Har-Shai Y, Bodner S, Egozy-Golan D, Lindenbaum E, Ben-Izhak O, Mitz V, Hirshowitz B. Mechanical properties and microstructure of the superficial musculoaponeurotic system, 1996.
64. Taylor RL, Simo JC, Zienkiewicz OC, Chan ACH. The patch test- a condition for assessing FEM convergence. *International Journal for Numerical Methods in Engineering* 1986; **22**(1):39–62.
65. Babuška I, Narasimhan R. The Babuška-Brezzi condition and the patch test: an example. *Computer Methods in Applied Mechanics and Engineering* 1997; **140**(1):183–199.
66. Zienkiewicz OC, Taylor RL. The finite element patch test revisited a computer test for convergence, validation and error estimates. *Computer Methods in Applied Mechanics and Engineering* 1997; **149**(1):223–254.
67. Hendriks F, Brokken D, Oomens C, Bader D, Baaijens F. The relative contributions of different skin layers to the mechanical behavior of human skin in vivo using suction experiments. *Medical Engineering & Physics* 2006; **28**(3):259–266.
68. Iivarinen JT, Korhonen RK, Julkunen P, Jurvelin JS. Experimental and computational analysis of soft tissue mechanical response under negative pressure in forearm. *Skin Research and Technology* 2013; **19**(1):e356–e365.
69. Piérard GE, Piérard S, Delvenne P, Piérard-Franchimont C. In vivo evaluation of the skin tensile strength by the suction method: Pilot study coping with hysteresis and creep extension, 2013.
70. Piérard GE, Hermanns-Lê T, Piérard-Franchimont C. Scleroderma: skin stiffness assessment using the stress–strain relationship under progressive suction. *Expert Opinion on Medical Diagnostics* 2013; **7**(2):119–125.
71. Tarsi GM, Gould RA, Chung JA, Xu AZ, Bozkurt A, Butcher JT. Method for non-optical quantification of in situ local soft tissue biomechanics. *Journal of Biomechanics* 2013; **46**(11):1938–1942.
72. Abellan MA, Zahouani H, Bergheau J. Contribution to the determination of in vivo mechanical characteristics of human skin by indentation test, 2013.
73. Iivarinen JT, Korhonen RK, Jurvelin JS. Experimental and numerical analysis of soft tissue stiffness measurement using manual indentation device: significance of indentation geometry and soft tissue thickness. *Skin Research and Technology* 2013:1–8. article in press.
74. Bhushan B, Tang W, Ge S. Nanomechanical characterization of skin and skin cream. *Journal of Microscopy* 2010; **240**(2):135–144.
75. Flynn C, Taberner A, Nielsen P. Mechanical characterisation of in vivo human skin using a 3D force-sensitive micro-robot and finite element analysis. *Biomechanics and Modeling in Mechanobiology* 2011; **10**(1):27–38.
76. Jor JWY, Nash MP, Nielsen PMF, Hunter PJ. Estimating material parameters of a structurally based constitutive relation for skin mechanics. *Biomechanics and Modeling in Mechanobiology* 2011; **10**(5):767–778.
77. Kathyr F, Imberdis C, Vescovo P, Varchon D, Lagarde J. Model of the viscoelastic behaviour of skin in vivo and study of anisotropy. *Skin Research and Technology* 2004; **10**:93–103.
78. Delalleau A, Josse G, Lagarde M, Zahouani H, Bergheau J. Characterization of the mechanical properties of skin by inverse analysis combined with the indentation test. *Journal of Biomechanics* 2006; **39**:1603–1610.
79. Diridollou S, Patat F, Gens F, Vaillant L, Black D, Lagarde JM, Gall Y, Berson M. In vivo model of the mechanical properties of the human skin under suction. *Skin Research and Technology* 2000; **6**(4):214–221.
80. Khatyr F, Imberdis C, Varchon D, Lagarde J, Josse G. Measurement of the mechanical properties of the skin using the suction test. *Skin Research and Technology* 2006; **12**:24–31.
81. Tran HV, Charleux F, Rachik M, Ehrlacher A, Ho Ba Tho MC. In vivo characterization of the mechanical properties of human skin derived from MRI and indentation techniques. *Computer Methods in Biomechanics and Biomedical Engineering* 2007; **10**(6):401–407.
82. Pailler-Mattei C, Nicoli S, Pirot F, Vargiolu R, Zahouani H. A new approach to describe the skin surface physical properties in vivo. *Colloids and Surfaces B: Biointerfaces* 2009; **68**(2):200–206.
83. Weickenmeier J, Itskov M, Mazza E, Jabareen M. A physically motivated constitutive model for 3D numerical simulation of skeletal muscles. *International Journal for Numerical Methods in Biomedical Engineering* 2014; **30**(5):545–562.
84. Mazza E, Papes O, Rubin M, Bodner S, Binur N. Simulation of the aging face. *Journal of Biomechanical Engineering* 2007; **129**(4):619–623.

DOI: 10.1002/cnm